CONTENTS

3 RESULTS AND DISCUSSION

APPENDIX A: Materials Joining Work Reports – Task IIA
APPENDIX B: Materials Joining Work Reports – Task IIB

1 BACKGROUND

The JIP wet welding consumables development project was undertaken with the objective to improve the quality of wet welds by optimization of coating composition. An organized, stepwise approach to coating formulation was chosen so that the influence of each individual ingredient could be understood.

Phase I of the project, which was completed in November of 1994, focused on optimizing the flux system by incrementally changing the content of the mineral ingredients of the coating. The result of Phase I was the development of a flux system which was capable of producing mechanical properties of 80 ksi tensile strength, 10 to 14% elongation, and 30 ft.-lb. @28 F Charpy impact toughness at a depth of 33 ft.

The objective of Phase II is to mitigate the adverse effects of increased pressure by optimizing the ferro-alloy content of the coating. It is known that increasing depth, and therefore hydrostatic pressure, has several adverse effects on wet weld quality. Weld metal oxygen and carbon increase with depth while manganese, silicon, and other elements with an affinity for oxygen decrease with depth. With the reduction in hardenability due to oxidation, coarse-grained primary ferrite (PF) replaces acicular ferrite (AF) and ferrite with second phase (FS) in the microstructure. Porosity also increases with depth. These trends are illustrated in the Interim Report contained in Appendix A of the Task I report. The net effect is a deterioration of weld metal mechanical properties with increasing depth. In Phase II, the target depth range of 0 to 300 feet is divided into four depths: 70, 140, 200, and 300 ft. for the purpose of testing and optimization. For each incremental increase in depth, ferro-alloy content of the coating is adjusted in an effort to replenish the alloying element loss from the weld pool with increasing depth.

Phase II is divided into four tasks. Task I involves optimization of the coating Fe-Mn content. Task II involves addition of titanium and boron to the coating to promote acicular ferrite in the microstructure. The results of Task II will be presented in this report. Task III involves addition of Rare Earth Metal (REM) to the coating in order to reduce oxygen content and improve toughness. Task IV involves characterizing the effects of the ferro-alloy additions on the reheated microstructure in multipass welds. Task IV is ongoing, and results are presented in the Task I and Task II reports.

The effect of ferro-manganese addition was initially tested on several different flux systems in Phase I. Fe-Mn was added in the amount of 8, 12, and 14 wt. pct. to the coating, and welds were made at 33 ft. depth. Increasing Fe-Mn in the coating produced mixed results. Mechanical properties were improved in some cases and made worse in others. It was apparent from the phase I results that there is an optimum addition of Fe-Mn which produces the best weld metal properties for a given flux system. Therefore, Task I of Phase II was undertaken to optimize Fe-Mn addition to the coating for the chosen flux system at each depth.

Task I was completed and a report was issued in November of 1998. The most significant results from Task I were:

- Weld metal manganese content was generally increased over the baseline data.

- Porosity was reduced over the baseline data. V-groove welds acceptable to AWS D3.6 class B, in terms of porosity, were produced at 70, 140, 200, and 300 ft. depths. Average porosity decreased slightly at each depth with increasing Fe-Mn in the coating.

- The 1F3 formulation at 70 ft. produced an ultimate tensile strength over 70 ksi, tensile elongation of 18.6%, and an average Charpy impact toughness of 28.6 ft.-lb. at 28 F. Charpy toughness is comparable to the welds made in Phase I at 33 ft., and tensile elongation is superior to any of the welds made in Phase I.

- Mechanical properties at 140 ft. were comparable in toughness and elongation to some of the Phase I welds made at 33 ft. Mechanical properties at 200, and 300 ft. were good for a first attempt, but typical of wet welds made at those depths in the past. Significant improvement in mechanical properties was achieved for 2F3 at 140 ft. on the second attempt, therefore further improvement in the properties may be possible.

The microstructure of the wet welds produced in Task I consisted mainly of coarse primary ferrite and ferrite with aligned carbides. In contrast, surface welds frequently contain large fractions of acicular ferrite, which is preferred due to the resistance of acicular ferrite to cleavage fracture. In a previous investigation at CSM, addition of titanium and boron to wet welding electrodes was shown to produce up to 60% acicular ferrite in the microstructure at a depth of 30 ft. (Sanchez-Osio 1995). It is not known if a microstructure high in acicular ferrite can be produced at greater depths, and mechanical testing was not performed in the previous investigation. The objective of Task II is to find Ti-B additions which will produce a microstructure high in acicular ferrite at each of the four depths and determine the effect on mechanical properties.

2 EXPERIMENTAL PROCEDURE

2.1 Formulation:

Preliminary steps were necessary to determine the recovery of titanium and boron from the coating to the weld metal in wet welding. Recoveries were approximated with data from Sanchez-Osio (1994), then four batches of experimental electrodes were produced at CSM. Wet welds were produced at CSM and evaluated in terms of microstructure and chemical composition. The results of this investigation were presented in the section "ONGOING TASKS" of the Task I report. One of the four formulations was selected for further trials. The formulation, referred to as T1B1, was used to product BOP-BOB welds at the four test depths by Global. The data from the T1B1 trial gave recoveries for titanium and boron at the four test depths, and allowed further development of the test matrix.

The preliminary test at CSM as well as data from Sanchez-Osio were used to quantify the interactive effect between Fe-Ti addition and the recoveries of manganese and boron. Titanium, being the strongest deoxidant in the system, protects manganese and boron from oxidation, thereby increasing their recoveries to the weld metal significantly. Whenever the Fe-Ti addition to the coating was increased, it was necessary to decrease the Fe-Mn and Fe-B additions in order to maintain a constant weld metal manganese and boron content. In order to compensate for the interactive effect, the effect of Fe-Ti addition on the manganese and boron recoveries was determined quantitatively. Recoveries of manganese and boron were plotted as a function of Fe-Ti addition, then a linear regression line was used to extrapolate or interpolate recoveries for Fe-Ti additions which had not yet been tried. Fe-Mn and Fe-B additions could then be adjusted to produce a constant weld metal manganese and boron content with increasing Fe-Ti addition.

In the next trial, two additional levels of boron and one increased level of titanium were tested at each depth. The entire remaining test matrix was not formulated at this point because there were only two data points at each depth from which to extrapolate recoveries, and considering the delicate balance of titanium, boron, and manganese which are required to produce the desired microstructure, it was concluded that an additional iteration would greatly increase the probability of success. Once the twelve experiments were analyzed, there was enough data to complete the test matrix, and the final twenty formulations were blended.

Due to the strong effect of titanium addition on the manganese recoveries, it was not possible to use the Fe-Mn additions developed for each depth in Task I. Instead, a weld metal manganese content of 0.6 to 0.7 was selected as the objective, and Fe-Mn additions were adjusted taking the Fe-Ti addition into account to give the desired weld metal manganese content. The weld metal manganese content was selected to give an as-deposited hardness of 200 to 300 HV. Hardness levels in Task I were generally less than 200 HV. A somewhat higher hardness was desirable to increase the strength of the Task II welds over the Task I welds which had rather low strength (71, 65, 53, and 54 ksi). Hardness was limited on the high end by the AWS D3.6 specification, which requires a Class A weld to have a maximum hardness less than 325 HV. It has been reported in the literature that a minimum manganese addition is necessary for the intragranular nucleation of acicular ferrite to occur (Evans 1993). Therefore, the highest weld metal manganese content which would produce an acceptable hardness was selected to produce a high AF content.

The Task II test matrix and recoveries are given in Table 2.1. Recovery is defined as the alloy content in the weld metal (wt. pct.) divided by the ferro-alloy addition to the coating (wt. pct.) multiplied by 100. The recoveries in Table 2.1 were calculated from the chemical analyses of the weld metal after the experiments were performed. In some cases, preliminary designations were given to formulations before the matrix was completely developed. Those designations are given in parentheses.

One formulation for each depth was selected from the Task IIA test matrix for the Task IIB V-groove welds. The criteria for the decision were hardness, porosity, and microstructure. First, all formulations which produced excessively hard deposits were eliminated. Maximum hardness is limited to 325 HV according to AWS D3.6. Next, the formulations which produced the lowest levels of porosity for a given depth were selected. Finally, among the formulations which produced acceptable hardness and low porosity, the one with the most favorable microstructure was selected. It was not necessary to extrude another batch of electrodes for the V- groove experiments as sufficient leftovers were available from Task IIA.

Table 2.1: Task IIA Test Matrix and Recoveries

	Fe-Mn		Fe-Ti		Fe-B	
	wt. pct.	Mn recovery (%)	wt. pct.	Ti recovery (%)	wt. pct.	B recovery (%)
1T1B1	14.5	**5.9**	5.0	**0.25**	0.5	**0.38**
1T1B2 (T1B1)	14.5	**5.0**	5.0	**0.62**	0.9	**0.21**
1T1B3	14.5	**6.2**	5.0	**0.30**	1.2	**0.41**
1T2B1	10.5	**5.8**	10.0	**0.17**	0.2	**0.40**
1T2B2(1T2BA)	12.4	**6.7**	10.0	**0.28**	0.4	**0.53**
1T2B3	10.5	**6.4**	10.0	**0.18**	0.6	**0.41**
1T3B1	8.5	**7.7**	15.0	**0.20**	0.2	**0.61**
1T3B2	8.5	**7.8**	15.0	**0.27**	0.4	**0.63**
1T3B3	8.5	**7.8**	15	**0.18**	0.5	**0.58**
2T1B1	16.0	**5.9**	5.0	**0.38**	0.5	**0.44**
2T1B2 (T1B1)	14.5	**4.8**	5.0	**0.66**	0.9	**0.22**
2T1B3	16.0	**6.0**	5.0	**0.30**	1.2	**0.39**
2T2B1	10.6	**6.3**	10.0	**0.72**	0.2	**0.50**
2T2B2 (2T2BA)	13.2	**6.6**	10.0	**0.20**	0.4	**0.54**
2T2B3	10.6	**5.8**	10.0	**0.17**	0.6	**0.33**
2T3B1	12.5	**5.0**	7.5	**0.19**	0.2	**0.30**
2T3B2	12.5	**4.6**	7.5	**0.21**	0.5	**0.28**
2T3B3	12.5	**5.8**	7.5	**0.26**	0.7	**0.40**
3T1B1	15.4	**4.7**	5.0	**0.46**	0.5	**0.23**
3T1B2 (T1B1)	14.5	**4.8**	5.0	**1.60**	0.9	**0.19**
3T1B3	15.4	**4.5**	5.0	**0.23**	1.3	**0.28**
3T2B1	11.3	**4.7**	10.0	**0.28**	0.2	**0.30**
3T2B2 (3T2BA)	13.1	**6.2**	10.0	**0.22**	0.4	**0.50**
3T2B3	11.3	**4.6**	10.0	**0.29**	0.6	**0.28**
3T3B1	12.5	**2.6**	7.5	**0.72**	0.3	**0.28**
3T3B2	12.5	**3.9**	7.5	**0.32**	0.5	**0.24**
3T3B3	12.5	**4.8**	7.5	**0.22**	0.8	**0.29**
4T1B1 (T1B1)	14.5	**4.7**	5	**2.20**	0.85	**0.14**
4T1B2	15	**4.6**	5	**0.48**	1.2	**0.30**
4T1B3	15	**5.1**	5	**0.69**	1.8	**0.26**
4T2B1	13.8	**5.3**	10	**0.21**	0.25	**0.40**
4T2B2 (4T2BA)	13.8	**4.3**	10	**0.13**	0.46	**0.28**
4T2B3	13.8	**7.5**	10	**0.44**	1	**0.30**
4T3B1	15	**3.1**	2.5	**1.30**	0.7	**0.14**
4T3B2	15	**3.8**	2.5	**1.46**	1.4	**0.20**
4T3B3	15	**3.9**	2.5	**0.94**	2.8	**0.27**

2.2 Electrode Production:

The coating ingredients were purchased from Cor-Met in Brighton, MI. The composition of the ferro-alloys from the material certification reports is given in Table 2.2.1. Coating ingredients were shipped to CSM where the dry mix was made. Mixing was performed in a V-blender with ceramic balls for at least 2 hours. The dry mix was returned to Cor-Met for extrusion. Cor-Met added approximately 10 wt. pct. potassium silicate as a binder and extruded the flux onto a 1/8 inch diameter steel core wire. The composition of the core wire is given in Table 2.2.2. The extruded rods were baked at 190 C for one hour to remove moisture and shipped to Global Industries in New Iberia, LA. Global performed a low temperature bake on the rods to remove any absorbed moisture and applied a water-proof coating.

2.3 Welding:

BOP-BOB welds were produced with nine formulations at each of the four test depths. The welds were produced by Global in a hyperbaric chamber pressurized to simulate the appropriate underwater depth. The set of experiments with the T1B1 formulation were deposited using a gravity-welding apparatus. All other experiments were deposited manually due to difficulties with the gravity apparatus. The base metal is a low carbon-manganese steel, the composition is listed in Table 2.2.2. A three-layer deposit scheme was used, consisting of four beads in the first layer, three in the second, and two in the final layer.

After analysis of the BOP-BOB welds, one composition was selected for each depth, and V-groove welds were prepared. The base metal was a 1-inch thick API 2W Grade 50 plate. The weld preparation was a 5/8 inch deep V-groove with a 60 degree included angle. Approximately 24 passes were required to complete the weldment. The V-groove welds were completed manually at Global's hyperbaric facility. Details of the welding procedure are given in the Materials Joining Work Reports from Global, attached as Appendix B.

Table 2.2.1: Composition of Ferro-Alloys (wt. pct.)

	Ti	Si	Mn	Al	B	C	P	S	Fe
Fe-Mn	--	0.75	88.95	--	--	0.145	0.186	0.008	bal.
Fe-Ti	38.14	0.61	--	2.93	--	0.170	0.120	0.027	bal.
Fe-B	--	0.80	--	0.21	17.50	0.260	0.018	0.004	bal.

Table 2.2.2: Base Metal and Core Wire Compositions

	C (wt. pct.)	Mn (wt. pct.)	Si (wt. pct.)	Ti (ppm)	B (ppm)
BOP-BOB	0.18	0.8	0.21	<100	<5
V-Groove	0.14	1.51	0.4	<100	5
Core wire	0.01	0.15	0.02	<100	<5

2.4 Radiography:

Radiography of the V-groove welds was supplied by Global from an independent testing facility. The welds were interpreted to AWS D3.6 by an ASNT level II inspector.

2.5 Metallography:

Area fraction of porosity and top bead microstructure were quantified using standard metallographic techniques. Two cross-sections from each weld were examined. Area fraction porosity was measured at 10x magnification by overlaying a transparent grid of 1mm squares on a photomicrograph and counting the number of squares over pores divided by the total number of squares over the weld metal. Four areas were analyzed. The average and 90% confidence interval of the four measurements were reported.

Top bead microstructure was examined at 500x magnification with a 2% nital etch. A total of ten photomicrographs was examined from each weld, three from each of two cross-sections. The microstructures were classified according to the IIW classification scheme for steel weld metal into PF (primary ferrite), FS (ferrite with second phase aligned or non-aligned), and AF (acicular ferrite). A one thousand point count on each weld, based on two cross-sections, was used to quantify the proportions of the different microstructural constituents.

A quantitative survey of the micro-cracking was conducted on the metallographic specimens by examining 100 fields at 200x on each cross-section and counting the number of fields containing micro-cracks vs. the number of fields which were free of cracks. Two cross-sections from each weld were examined. The data was reported as a percentage by dividing the number of fields containing cracks over the total number of fields examined.

2.6 Chemical Analysis:

The chemical analysis procedure was modified from Task I for improved accuracy and confidence. Weld metal chemical compositions were measured by an independent lab in Denver, CO using optical emission spectroscopy. It was found that porosity on the surface to be examined significantly influenced the results. A procedure was developed which produces a flat surface on the top bead by peening with a ball-peen hammer, then grinding lightly to clean up the surface. In Task I, the flat surface for analysis was produced by grinding alone, which often led to complete removal of the top bead and exposure of sub-surface porosity. The new procedure produces a flat, pore-free surface on the top layer of the deposit, resulting in a more accurate analysis. In addition, a deposit scheme which uses two beads in the top layer was adopted, so that the chemical analysis could more easily be performed on the top layer. Finally, two locations from each weld were tested, instead of one in Task I, and the average reported.

Oxygen and nitrogen were measured at Colorado School of Mines by combustion analysis with a Leco oxygen/ nitrogen analyzer. As in Task I, five specimens from each weld were tested to give a reasonable level of confidence. The average and 90% confidence interval were reported.

2.7 Hardness

Vickers microhardness measurements were made to determine the hardness of the top-bead microstructure. A 1 kg load was used in order to make an indentation that was larger than the individual microstructural constituents and give an average hardness. Five indentations were made on each of the two metallographic mounts from each experiment resulting in a total of ten measurements from each weld. The average, maximum, and 90% confidence interval were reported.

2.8 Mechanical Testing:

Results of all-weld-metal tensile tests and Charpy V-notch impact toughness tests were supplied by Global from an independent lab. Full size Charpy bars and tensile bars with a 1/4 inch round reduced section were used. Charpy impact tests were performed at 28 F, in accordance with AWS D3.6.

3 RESULTS AND DISCUSSION

3.1 Results of Task II Experiments:

The results of the Task II Experiments are presented in Tables 3.1.1, 3.1.2, and 3.1.3. Mechanical testing results from Task IB are included in Table 3.1.4 for comparison.

Table 3.1.1: Results of Task IIA BOP-BOB Experiments

	Fe-Mn	Fe-Ti	Fe-B	Mn	Ti	B	O		N		Hardness			Porosity		Microstructure		
	wt. pct.			wt. pct.	ppm	ppm	ppm	+/-	ppm	+/-	avg	+/-	max	avg	+/-	PF	FS	AF
1T1B1	14.5	5.0	0.5	0.86	125	18	875	7	61.9	0.3	304	5	322	0.6	0.5	20	3	77
1T1B2	14.5	5.0	0.9	0.72	310	18	912	124	89.0	2.8	301	12	340	1.1	0.5	10	1	90
1T1B3	14.5	5.0	1.2	0.91	150	48	887	29	63.8	0.5	321	7	340	0.8	0.2	5	40	55
1T2B1	10.5	10.0	0.2	0.61	165	8	966	76	84.2	0.8	283	6	302	1.9	0.9	30	10	60
1T2B2	12.4	10.0	0.4	0.83	280	20	797	25	76.0	0.6	305	4	316	0.7	0.2	15	4	81
1T2B3	10.5	10.0	0.6	0.67	175	25	1005	46	102.0	1.4	277	6	297	2.2	0.4	18	2	82
1T3B1	8.5	15.0	0.2	0.66	305	11	929	29	88.9	1.2	296	7	317	3.7	0.8	11	3	86
1T3B2	8.5	15.0	0.4	0.66	400	22	911	48	107.9	1.6	292	7	311	4.7	1.7	10	2	89
1T3B3	8.5	15.0	0.5	0.67	265	29	934	35	109.3	1.0	288	5	302	4.2	2.0	12	2	87
2T1B1	16.0	5.0	0.5	0.95	190	21	937	30	72.5	2.1	329	9	361	1.4	0.6	10	3	87
2T1B2	14.5	5.0	0.9	0.70	330	19	1012	38	86.1	1.4	274	7	290	2.4	0.5	19	2	78
2T1B3	16.0	5.0	1.2	0.97	150	46	866	28	73.1	1.3	362	8	388	1.2	0.6	4	68	28
2T2B1	10.6	10.0	0.2	0.67	720	10	1317	95	95.5	0.9	279	8	297	4.2	0.5	30	12	58
2T2B2	13.2	10.0	0.4	0.87	200	21	856	42	69.6	1.3	320	5	336	1.9	0.6	15	4	81
2T2B3	10.6	10.0	0.6	0.62	165	20	1264	54	94.7	0.9	286	12	311	4.6	0.7	13	1	86
2T3B1	12.5	7.5	0.2	0.63	145	7	942	46	77.2	0.9	258	8	289	2.3	0.3	32	38	31
2T3B2	12.5	7.5	0.5	0.58	160	13	1222	28	71.1	1.9	268	7	300	2.5	0.9	28	10	62
2T3B3	12.5	7.5	0.7	0.73	195	27	1086	52	75.7	0.9	280	9	301	1.7	0.5	23	2	76
3T1B1	15.4	5.0	0.5	0.73	230	12	1039	27	69.6	1.6	288	6	313	1.4	0.4	21	18	62
3T1B2	14.5	5.0	0.9	0.70	800	16	1231	32	83.2	1.7	280	12	316	3.4	1.3	16	1	83
3T1B3	15.4	5.0	1.3	0.70	115	36	1003	58	69.8	2.6	305	12	343	2.1	1.0	7	38	56
3T2B1	11.3	10.0	0.2	0.53	275	6	1589	132	106.1	1.1	266	9	291	4.7	1.0	30	13	57
3T2B2	13.1	10.0	0.4	0.81	220	20	1068	81	71.9	1.8	342	18	401	4.4	1.4	15	9	76
3T2B3	11.3	10.0	0.6	0.52	290	17	1348	179	96.1	5.9	301	6	314	4.5	0.3	17	1	82
3T3B1	12.5	7.5	0.3	0.32	540	9	1485	71	64.6	1.3	268	8	291	3.8	0.7	29	32	37
3T3B2	12.5	7.5	0.5	0.49	240	12	1330	98	73.3	1.6	270	7	297	3.8	1.0	25	7	68
3T3B3	12.5	7.5	0.8	0.60	165	24	1411	66	74.8	0.9	294	13	345	5.4	1.5	17	3	79
4T1B1	14.5	5.0	0.9	0.68	1100	12	1969	139	92.5	4.9	242	9	275	8.0	2.4	31	11	59
4T1B2	15.0	5.0	1.2	0.69	240	37	1251	91	72.5	2.1	309	9	350	2.8	0.7	6	24	70
4T1B3	15.0	5.0	1.8	0.77	345	48	2097	756	72.7	2.0	361	10	386	5.0	0.5	2	85	14
4T2B1	13.8	10.0	0.3	0.74	210	10	1173	35	54.2	4.2	306	14	350	4.3	1.1	11	13	76
4T2B2	13.8	10.0	0.5	0.60	125	13	1750	500	74.7	2.1	329	6	357	9.5	1.2	13	9	78
4T2B3	13.8	10.0	1.0	--	435	30	1202	81	95.1	2.2	340	22	380	6.8	2.0	4	43	52
4T3B1	15.0	2.5	0.7	0.46	325	10	1366	112	85.3	7.1	247	8	283	2.7	1.3	30	57	12
4T3B2	15.0	2.5	1.4	0.57	365	29	1327	221	58.0	1.3	275	11	311	3.2	0.6	34	21	45
4T3B3	15.0	2.5	2.8	0.59	235	77	1317	243	58.9	1.1	314	9	343	4.8	1.2	2	94	4

Table 3.1.2: Results of Task IIB V-groove welds.

	Fe-Mn	Fe-Ti	Fe-B	Mn	Ti	B	O		N		Hardness				Porosity			Microstructure
	wt. pct.			wt. pct.	ppm	ppm	ppm	+/-	ppm	+/-	avg	+/-	max	avg	+/-	PF	FS	AF
1T2B2	12.4	10.0	0.4	1.03	330	22	818	19	91.3	0.8	296	13	325	0.8	0.3	12	0	88
2T3B3	12.5	7.5	0.7	0.51	95	14	1119	9	61.0	0.8	260	9	289	3.5	1.6	29	5	67
3T1B1	15.4	5.0	0.5	0.60	75	8	1180	70	78.0	1.1	286	9	308	1.8	0.4	18	8	74
4T3B2	15.0	2.5	1.4	0.48	145	20	1223	63	43.3	1.8	226	8	251	4.0	1.6	34	10	57

Table 3.1.3: Mechanical Testing Results from Task IIB V-groove Welds

		All Weld Metal Tensile			Charpy Toughness @28 F (ft.-lb.)			
Formulation	Depth (ft.)	Yield Stress (psi)	Ultimate Stress (psi)	Elongation (%)	Average	Min.	Max.	Shear (%)
1T2B2	70	66,692	71,231	4.2	22	21	24	90-100
2T3B3	140	77,698	80,038	3.7	26	24	30	100
3T1B1	200	63,750	67,500	6.4	22	22	22	100
4T3B2	300	56,830	60,189	8.7	20	19	20	100

Table 3.1.4: Mechanical Testing Results from Task IB V-groove Welds

		All Weld Metal Tensile			Charpy Toughness @28 F (ft.-lb.)			
Formulation	Depth (ft.)	Yield Stress (psi)	Ultimate Stress (psi)	Elongation (%)	Average	Min.	Max.	Shear (%)
1F3	70	64,313	71,098	18.6	29	28	30	90
2F3	140	56,440	64,640	11.7	25	23	28	100
3F3	200	53,440	58,520	3.6*	17 (23)	8 (22)	24	100
4F2	300	53,800	58,800	6.8	19	17	20	100

* The tensile bar fractured at a large pore.

( ) Values in parenthesis only consider the three Charpy bars without cracks.

3.2 Electrode Weldability:

Comments on electrode performance were provided in work reports from Global, which are attached as Appendix A. The comments of the diver/welders were mostly positive. In Task I, diver/welders noted that the slag was sometimes fluid and difficult to manage. Secondary slag adhesion was also noted. The comments from the Task II experiments indicated that slag removal was easy, and excessively fluid slag was not mentioned as a problem.

Experiments at CSM revealed a significant difference in the slag characteristics between Task I and Task II electrodes. The Task I electrodes produced a thin, crumbly slag which required wire-brushing for removal. Task II electrodes produced a thick, coherent slag layer which detached easily in large pieces.

3.3 Chemical Composition of Welds:

The results of Task IIA are summarized in Table 3.1.1. The addition of titanium had a strong effect on the recovery of both manganese and boron, as can be seen in Figures 3.3.1, 3.3.2, and Table 2.1. At 70 ft., manganese recovery increased from approximately 3.5 wt. pct. to nearly 8 wt. pct. with an increase in Fe-Ti addition from 0 to 15 wt. pct.. Boron recovery nearly doubled with an increase in Fe-Ti addition from 5 to 15 wt. pct.. Titanium, being the strongest deoxidant in the system, protects the other elements from oxidation. Thus a greater percentage of the ferro-alloy addition remains in the weld metal, rather than being oxidized and partitioned to the slag.

When the method of depositing the test welds was switched from mechanical to manual, a significant effect on the recoveries of boron and manganese was observed. In Table 2.1, the formulations labeled (T1B1) were deposited mechanically. The next set of formulations, appearing in boldface type, was deposited manually. For the same titanium addition, the boron recovery nearly doubled (approximately 0.2 to 0.4 % for 70 and 140 ft.). The effect was somewhat less significant at 200 ft., but the boron recovery nearly doubled again at 300 ft. The manganese recovery at 70 and 140 ft. increased by approximately 1% with the switch from mechanical to manual deposition, while the effect was minimal at 200 and 300 ft. In Table 3.1.1, the effects of the changes in recovery can be seen. For example, at 70 ft. 1T1B1 and 1T1B3 were formulated to give boron contents of 10 and 25 ppm with a manganese content of 0.7; however, the result was 18 and 48 ppm boron with 0.86 and 0.91 wt. pct. manganese due to the increased recoveries.

A significant decrease in oxygen content can be seen at 140 and 200 ft. with the switch from mechanical to manual deposition. At 70 ft. there was a reduction in average oxygen, but the reduction was not greater than the 90% confidence interval, and at 300 ft. there was a significant reduction in 4T1B2, but not in 4T1B3. There was also a tendency for porosity to decrease, especially at greater depths, with the change from mechanical to manual deposition. The increase in recoveries along with the decrease in oxygen content and porosity suggests that the weld pool is better protected from exposure to the water in the case of manual welding. A skilled diver/welder should be able to manipulate the electrode and maintain a short arc length better than a simple gravitational welding apparatus. The observation that the method of deposition, and by extension the skill of the diver/welder, can have a significant effect on chemical composition is important. In the case of micro-alloyed consumables, a small change in composition could have a large effect on the microstructure.

Weld metal oxygen content for Task IIA tended to be lower than Task IA for the 70 ft. BOP-BOB welds, but similar or even higher at greater depths. For the V-groove welds, Task IIB showed significantly lower oxygen contents at all depths than Task IB welds, as seen in Figure 3.3.3.

Weld metal Nitrogen content was measured and reported as a quality control measure. Both Fe-titanium and Fe-B can absorb nitrogen from the atmosphere in storage and deliver it to the weld metal. Excessive nitrogen in the weld metal can form porosity and embrittling nitrides. Nitrogen values were all at low enough levels that nitrogen porosity and nitrides should not pose a problem.

The chemical compositions of the V-groove welds did not exactly match the corresponding

BOP-BOB experiments even though both were deposited manually from the same batches of electrodes. Referring to Tables 3.1.1 and 3.1.2, it can be seen that the manganese content of the 1T2B2 deposit was 0.83 wt. pct. in the BOP-BOB experiment, whereas it was 1.03 wt. pct. in the V-groove experiment. In the other three cases, the manganese, titanium, and boron levels were less in the V-groove than in the BOP-BOB trial. It was mentioned previously that welder technique may have an influence on the recoveries of the alloying elements. It is possible that the variations are due to differences in welder technique. Another possible explanation is that the fluxes were not uniformly mixed. The reduction in alloy recovery for the 140, 200, and 300 ft. experiments is consistent for manganese, titanium, and boron, which favors the welder technique explanation. Non-uniform mixing of the flux would be expected to produce random increases and decreases in each of the three alloying elements rather than having the three elements increase or decrease together.

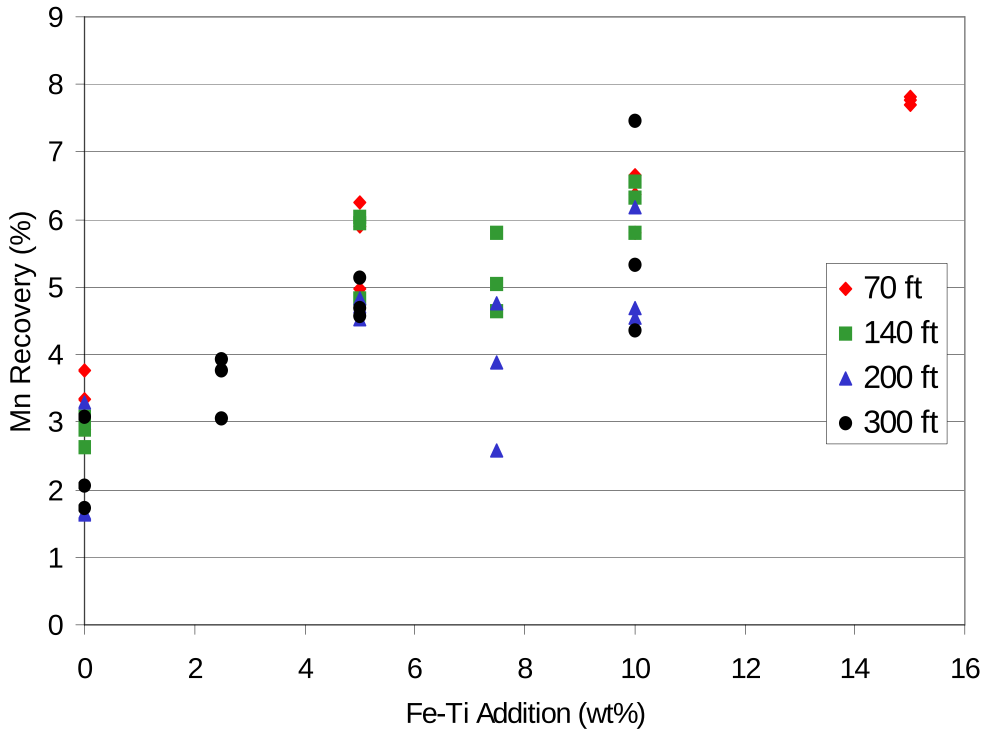

Figure 3.3.1: Manganese Recovery vs Fe-Mn Addition

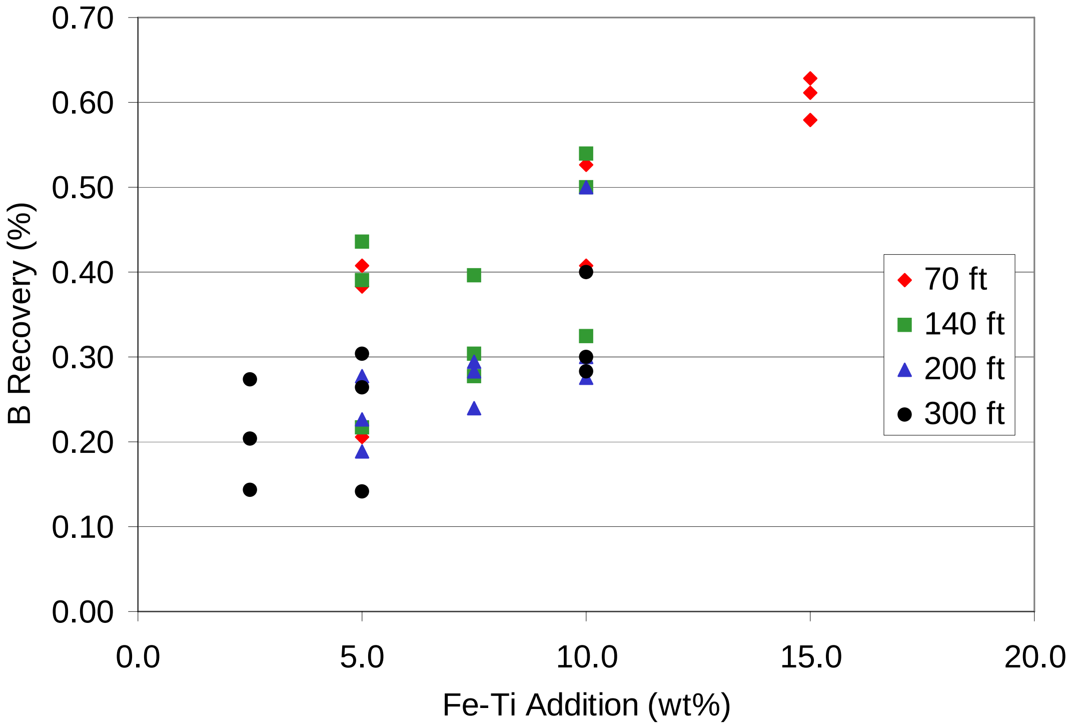

Figure 3.3.2: Boron Recovery vs Fe-Ti Addition

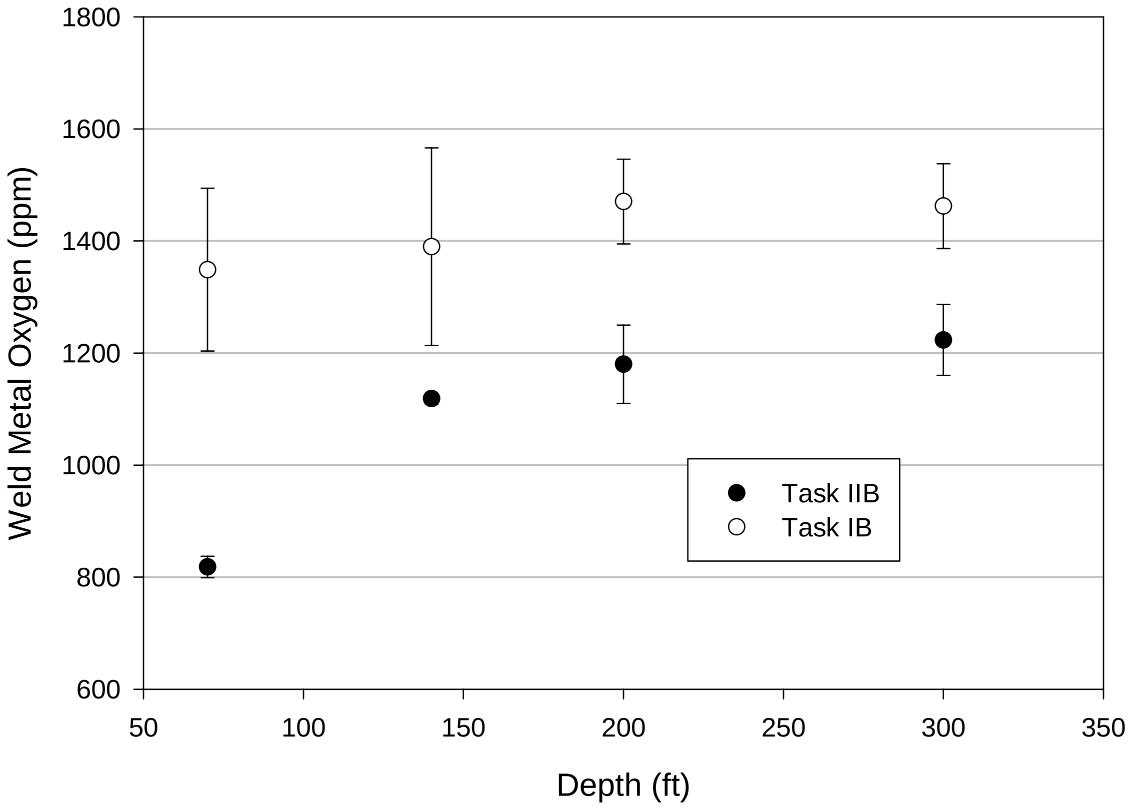

Figure 3.3.3: Weld metal oxygen vs. depth for Task I and Task II V-groove welds.

3.4 Porosity:

Porosity had a tendency to increase as a function of increasing titanium and boron additions. As seen in Figure 3.4.1. The data plotted in Figure 3.4.1 are from welds which were all deposited manually in the same batch.

Some information on the sources of porosity in underwater wet welds can be found in the literature. Suga (1986) reported that the composition of gas contained in wet weld porosity is 96% hydrogen with a small amount of carbon monoxide. Liu et al (1994) investigated the chemical reactions that could cause porosity formation in wet welds by means of thermodynamic calculations. Oxygen and hydrogen are present in the arc atmosphere due to the dissociation of water in the arc, and are dissolved into the weld pool at high temperatures. The solubility of both oxygen and hydrogen in the weld pool decreases as the liquid metal cools and solidifies. Oxygen can come out of solution by reacting with carbon to produce carbon monoxide porosity. Liu et al (1994) suggested that the oxygen can also react with hydrogen to produce steam porosity. Liu et al (1994) went on to suggest that steam in the pores can react with the surrounding iron to form iron oxide and hydrogen, thus explaining the presence of hydrogen, and not steam, in the pores. The other possibility is that hydrogen dissolved in the weld pool forms porosity by re-combination into molecular hydrogen. Liu et al (1994) suggested that if the weld pool were sufficiently deoxidized, porosity due to both carbon monoxide and steam could be prevented.

Figure 3.4.2 shows calculated values of oxygen dissolved in iron at equilibrium with various deoxidants in the weld pool. It is important to note that the Y-axis is oxygen dissolved in the weld pool, and not oxygen in the form of oxide inclusions, which is measured by combustion analysis of the solidified weld metal. The oxygen content is limited by the element which has the lowest equilibrium value of dissolved oxygen. In a system with only manganese and carbon, the oxygen content is limited by carbon at higher temperatures and by manganese at lower temperatures; therefore, CO porosity would be possible. In a system that includes 200 ppm titanium, oxygen content is limited by the formation of titanium oxide, and CO formation is not possible. In the present investigation, increasing titanium additions produced more porosity, rather than less porosity as would be expected if porosity were caused by oxidation of carbon to form CO or hydrogen to form water vapor. Therefore, it is most likely that porosity in wet welds is caused by evolution of molecular hydrogen from the weld pool.

In Task I, it was noted that porosity decreased at each depth with increasing ferro-manganese addition, and in Task II, that porosity increased with increasing titanium and boron addition. These trends may be explained by the effect of slag composition on the absorption of hydrogen into the weld pool. Figure 3.4.3 gives data from steelmaking literature (Turkdogan 1983) on the effect of slag basicity on the solubility of water vapor in the slag. In many slag systems there is a minimum in water vapor solubility near neutral basicity. In welding literature, Surian (1997) and De Rissone et al (1997) have shown that increasing the slag basicity of rutile-base SMAW electrodes results in lower diffusible hydrogen for similar moisture contents. Medeiros (1998) has shown that diffusible hydrogen goes through a minimum with increasing additions of hematite to an acid electrode coating. Hematite decomposes to form FeO in the slag, thus increasing slag basicity. Medeiros noted a similar trend for total hydrogen content (diffusible plus residual). If porosity in wet welds is caused by hydrogen and weld metal hydrogen is affected by slag basicity, it can be expected that slag basicity will affect the amount of porosity in underwater wet welds. In Task I, it was noted that increasing Fe-Mn additions decreased porosity. Due to the oxidizing environment, most of the manganese addition partitions to the slag as MnO, a basic oxide which increases slag basicity. Titanium and boron are stronger deoxidants than manganese, and therefore protect manganese from oxidation. When titanium and boron are added, MnO content of the slag decreases and titanium oxide content of the slag increases, resulting in decreased slag basicity. Ferro-Manganese addition increases slag basicity, and therefore reduces porosity. Titanium and Boron addition reduce slag basicity, and therefore increase porosity.

Porosity had a tendency to be higher for mechanically deposited welds than for manually deposited welds. This observation is consistent with increased exposure to the water (oxygen and hydrogen) which leads to lower elemental recovery due to oxidation and higher porosity due to hydrogen. The same trend was noted in Task I where the porosity levels of the V-groove welds, which were manually deposited, were much lower than the porosity levels of the BOP-

BOB experiments, which were mechanically deposited, produced with the same formulations.

Porosity levels for the Task IIB V-groove welds were similar to the comparable BOP-BOB experiments with one exception. The 140 ft. weld had a porosity level approximately double that of the comparable BOP-BOB weld. This variation may be due to welder technique, which controls the exposure of the weld pool to the water. Figure 3.4.6 compares the porosity values of the Task IIB welds to those of the Task IIA welds. In most cases the porosity levels are somewhat higher with the notable exception of the 70 ft. weld, which had a very low level of porosity. It is not surprising that the porosity levels would be higher, considering that titanium and boron additions were shown to increase porosity; however, it was still possible to maintain porosity levels well below the 5% required for a Class B weld.

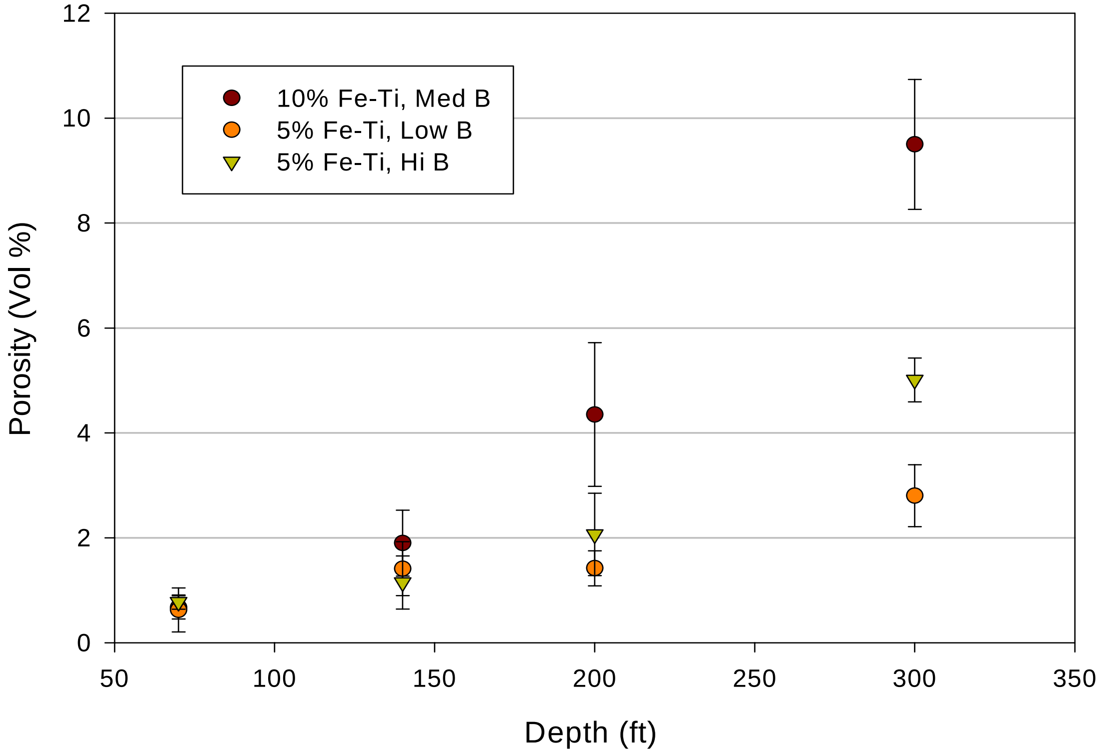

Figure 3.4.1: Porosity as a function of depth, Ti, and B addition.

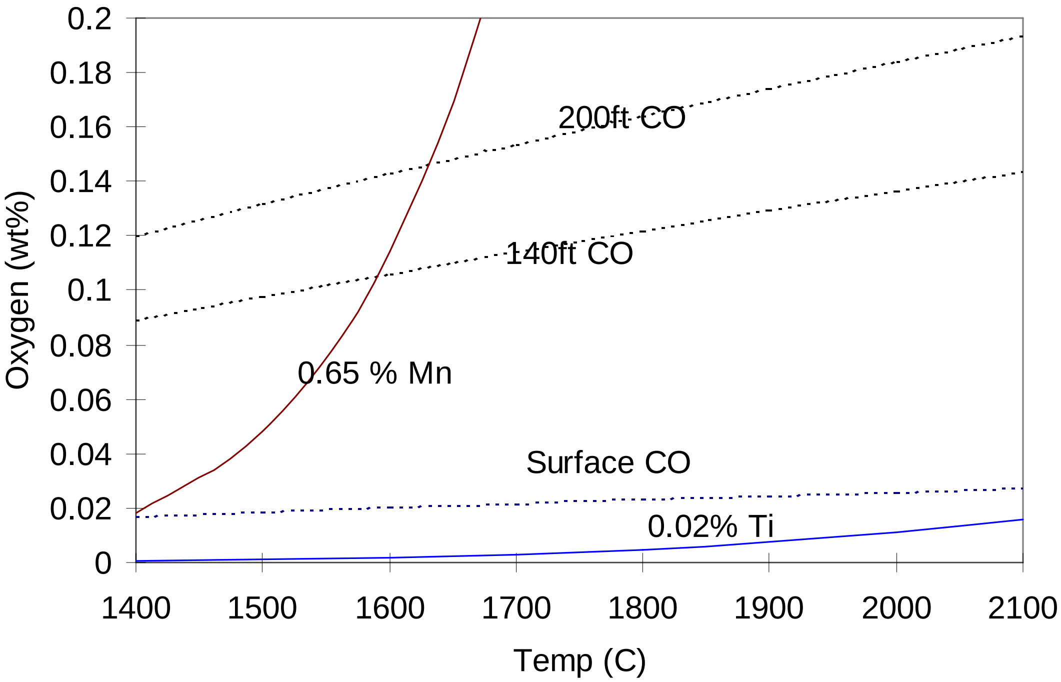

Figure 3.4.2: Weld metal oxygen in equilibrium with 0.05% C at various depths (assuming a pore composition of 50% hydrogen 50% CO), Mn with MnO, and Ti with Ti3O5

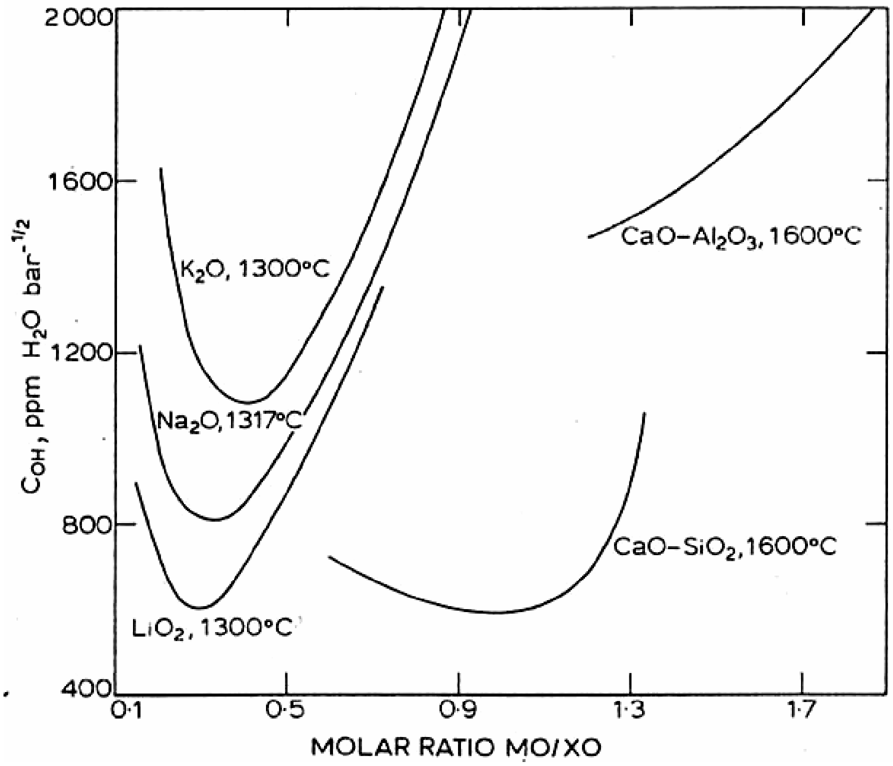

Figure 3.4.3: Water vapor solubility (C_{OH}) as a function of slag basicity (increasing basicity to the right)[5].

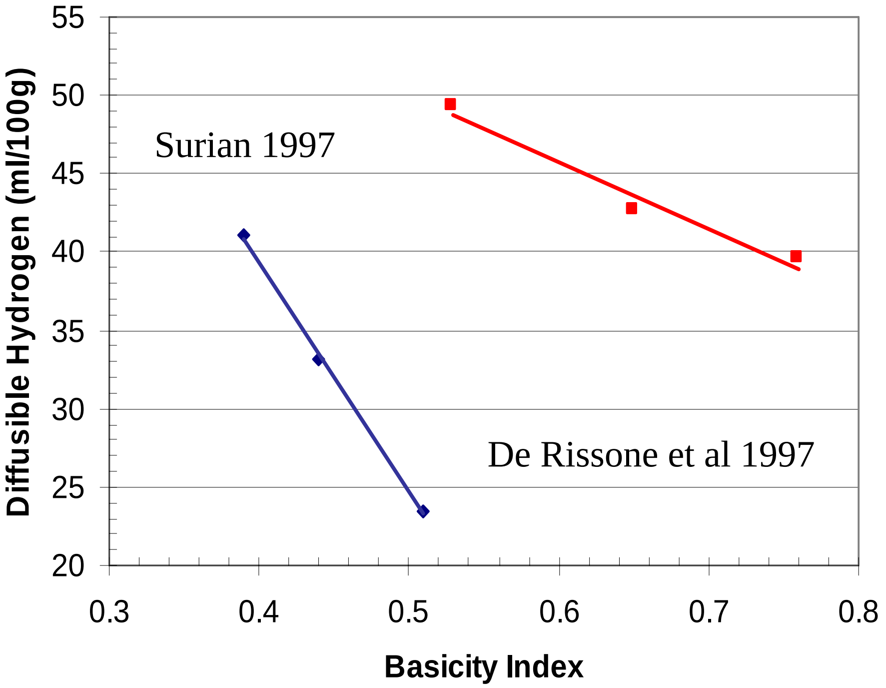

Figure 3.4.4: Diffusible hydrogen as a function of slag basicity for a rutile-base electrode deposited in air[6,7].

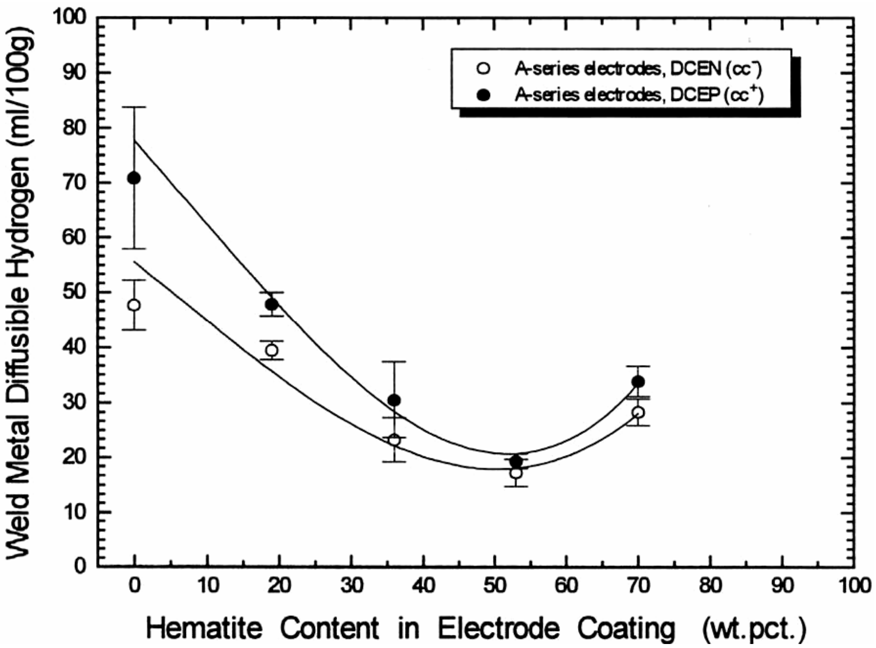

Figure 3.4.5: Diffusible hydrogen in underwater wet welds as a function of hematite content of the electrode coating. (Medeiros 1998).

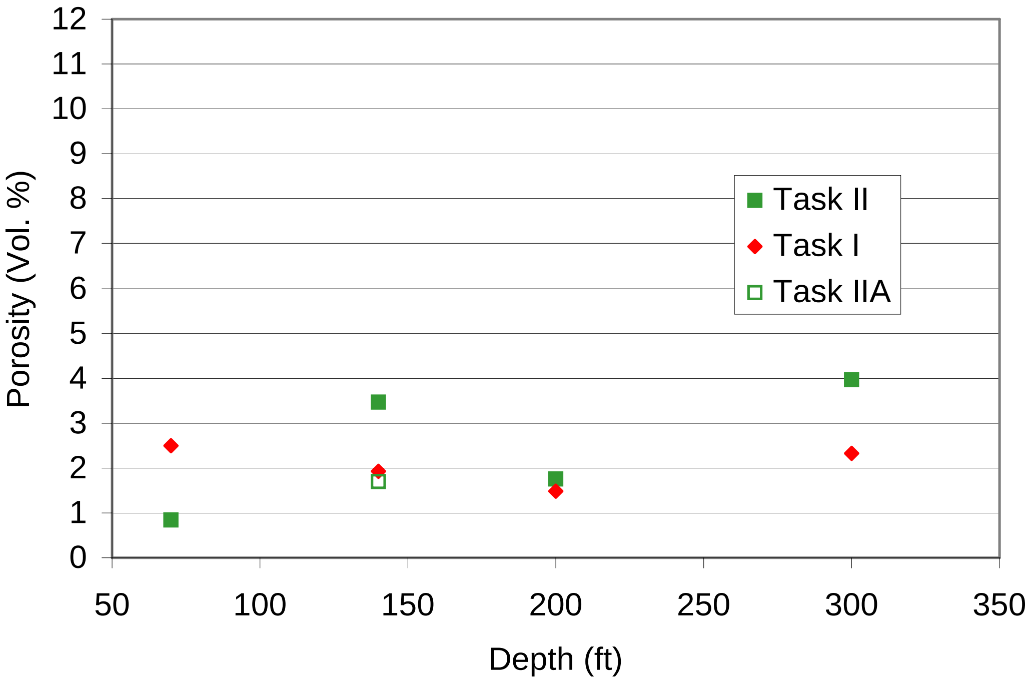

Figure 3.4.6: Porosity of Task I and Task II V-groove welds as a function of depth. The open square is the BOP-BOB experiment for 2T3B3 showing the unusually high value for the V-groove weld with the same composition.

3.5 Top Bead Microstructure

The Ti-B additions produced a substantial increase in the amount of acicular ferrite over the Task I welds. Results of the quantitative metallography are given in Table 3.1.1. The typical microstructure of the Task I welds consisted of 25-40% PF, 40-60% FS, and 10-20% AF. In Task IIA, microstructures containing 60-80% AF were produced at all four depths.

Figure 3.5.1 compares the acicular ferrite content of the top bead microstructures from Task I and Task II V-groove welds. A substantial increase in the acicular ferrite content was achieved by adding titanium and boron. Figures 3.5.2-5 show the macro-sections and top-bead microstructures from the four V-groove welds. Note the large fraction of acicular ferrite in the top bead microstructures.

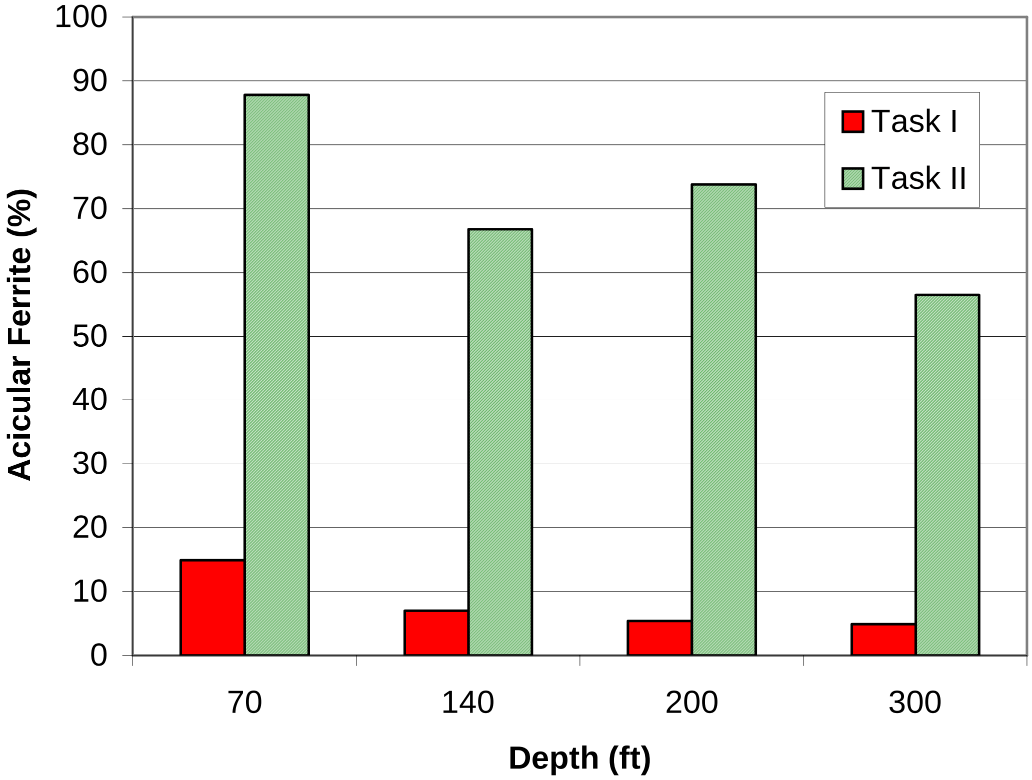

Figure 3.5.1: Percent acicular ferrite in the top bead microstructure vs. depth for Task I and Task II V-groove welds.

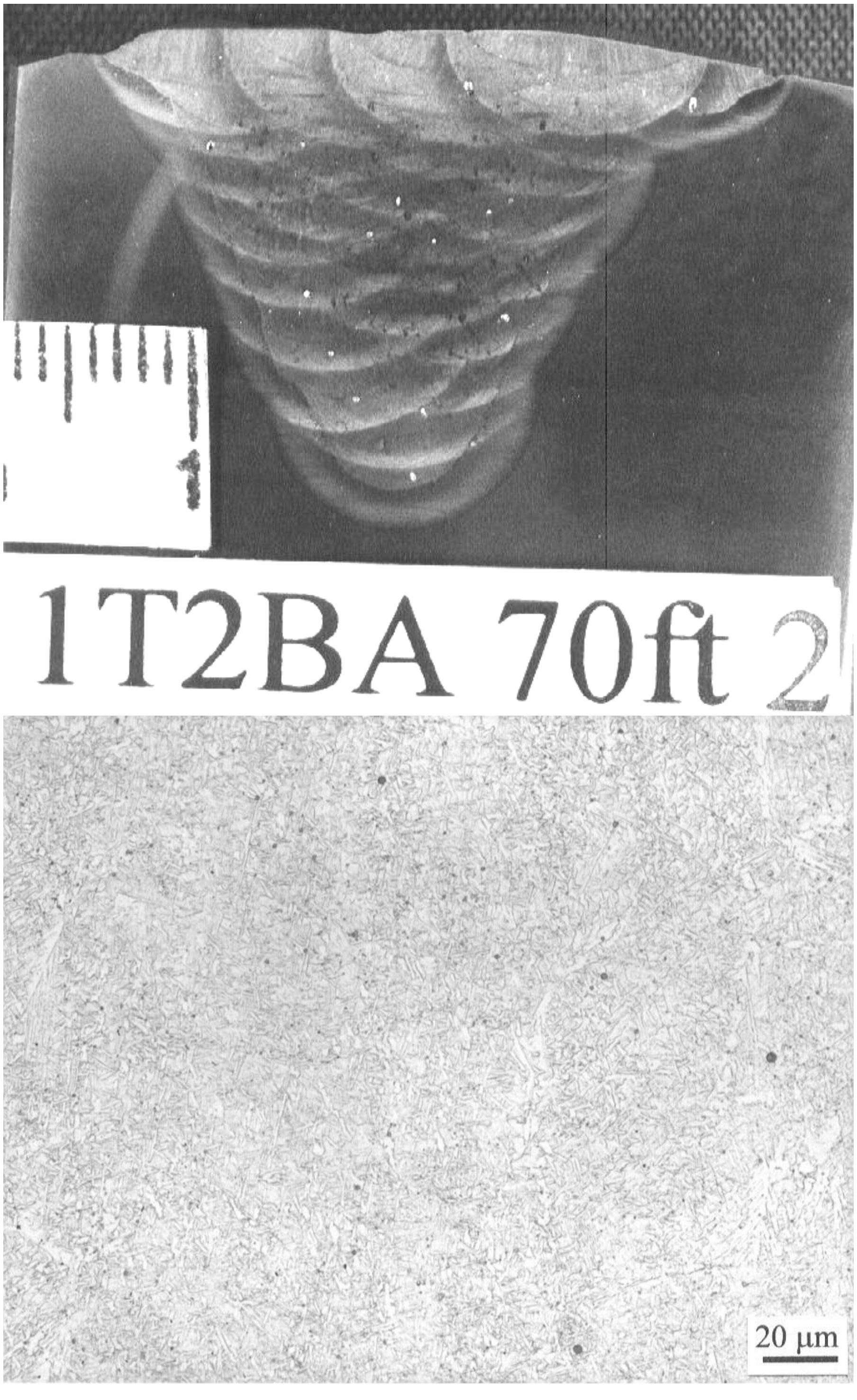

Figure 3.5.2: Macro-section and top bead microstructure from 1T2B2 V-groove weld.

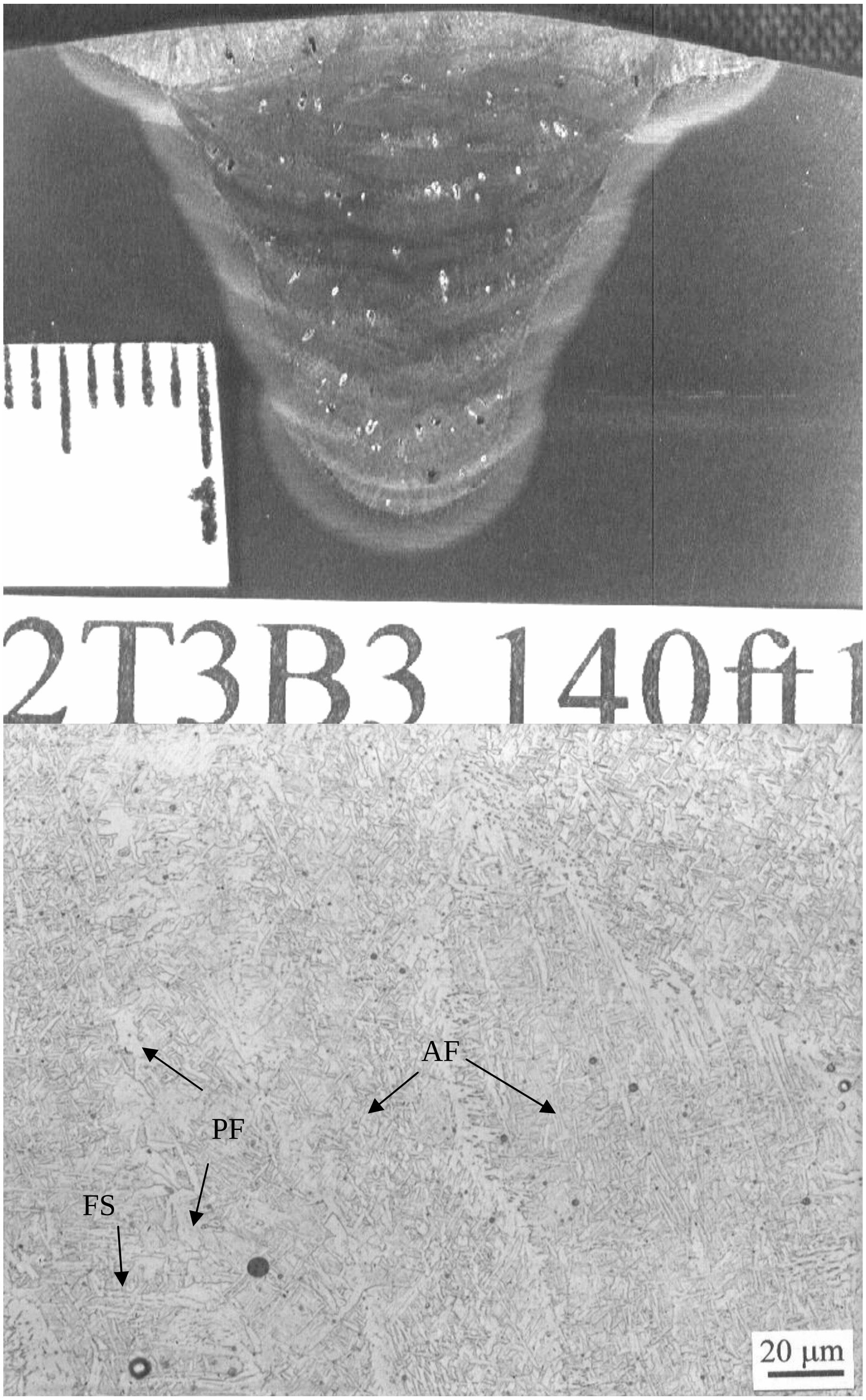

Figure 3.5.3: Macro-section and top bead microstructure from 2T3B3 V-groove weld.

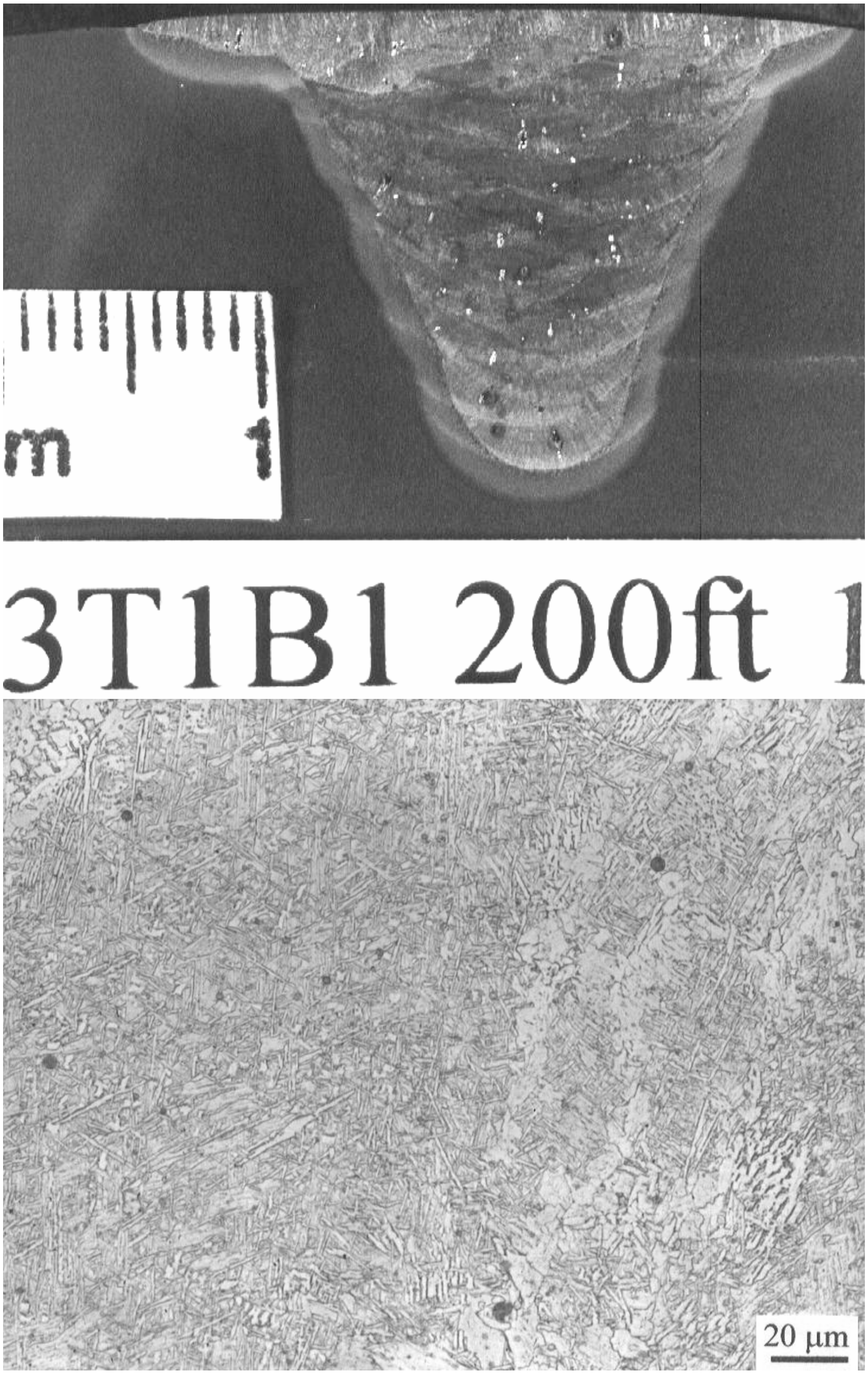

Figure 3.5.4: Macro-section and top bead microstructure from 3T1B1 V-groove weld.

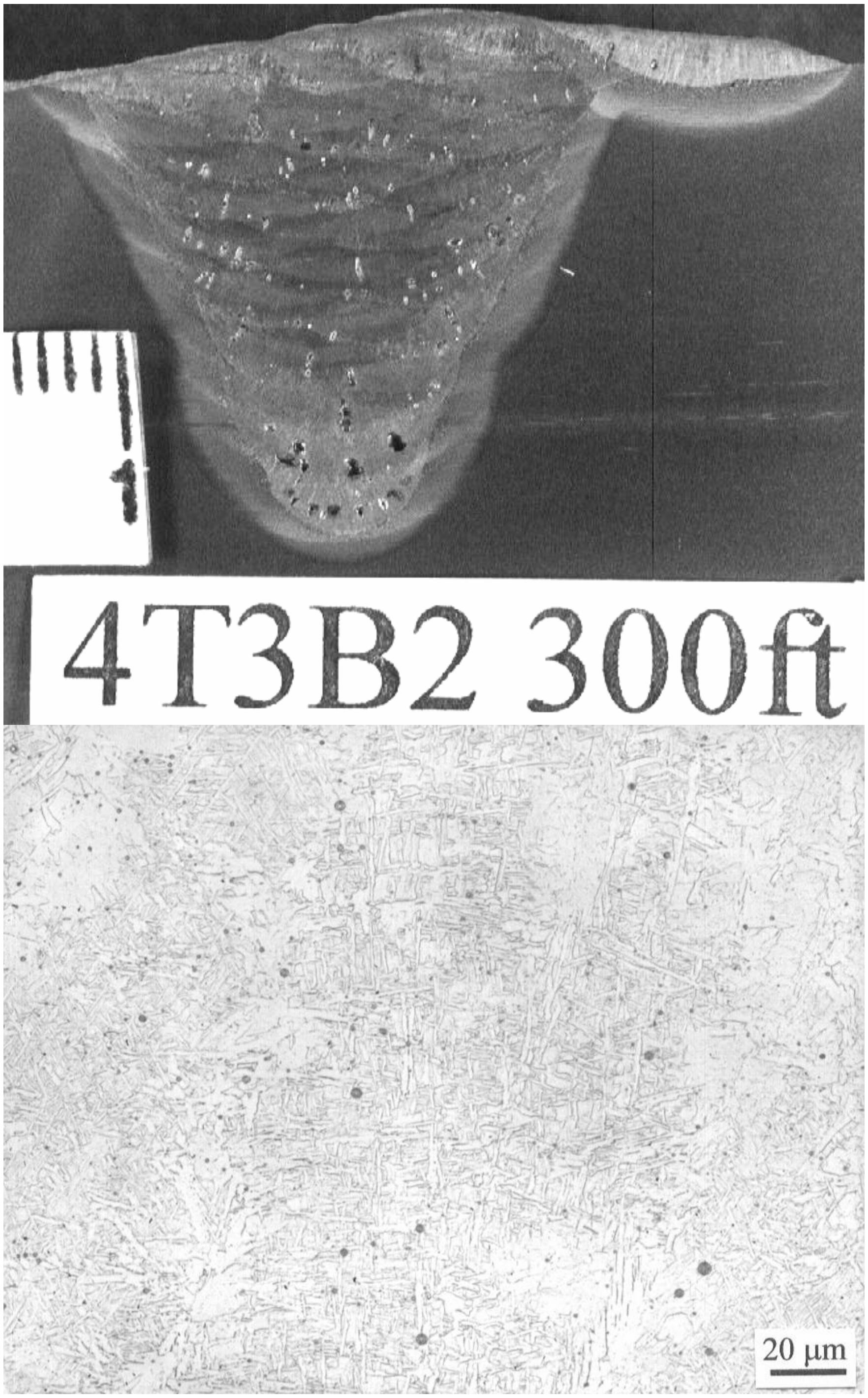

Figure 3.5.5: Macro-section and top bead microstructure from 4T3B2 V-groove weld.

3.6 Reheated Microstructure:

From the macrographs in Figures 3.5.2-5, it can be seen that the fraction of re-heated microstructure in the multipass welds is high; therefore, the mechanical properties are most likely influenced by the re-heated microstructure. Figures 3.6.1-2 compare reheated weld metal microstructures from Task I and Task II V-groove welds.

Significant microstructural refinement occurred in the coarse-grained reheated zone (CGRHZ) due to the Ti-B additions. The CGRHZ is heated high into the austenite phase field, and significant austenite grain growth results. On cooling, the austenite transforms back to ferrite. In the Task I welds, hardenability was very low, and the result was a microstructure of coarse PF with a small amount of FS, as seen in Figures 3.6.1-2 in the upper right. In the Task II welds the microstructure in the CGRHZ consisted of a much smaller amount of PF on the prior-austenite grain boundaries, and intragranularly nucleated AF and FS, as seen in Figures 3.6.1-2 in the upper left. Boron inhibited the nucleation of PF at the prior-austenite grain boundaries, while titanium-rich oxide inclusions provided intragranular nucleation sites for AF. The result was a much finer ferrite microstructure in the CGRHZ for Task II compared to Task I.

Microstructural refinement was also apparent in the fine-grained reheated zone (FGRHZ), although not to the same extent as in the CGRHZ, as seen in Figures 3.6.1-2 at bottom. The FGRHZ is heated to temperatures where partial transformation to austenite occurs, and there is no opportunity for austenite grain growth. The grain size in the FGRHZ is related to the as-deposited microstructure from which it originated. Refinement occurred due to the finer as-deposited microstructure in the Ti-B welds.

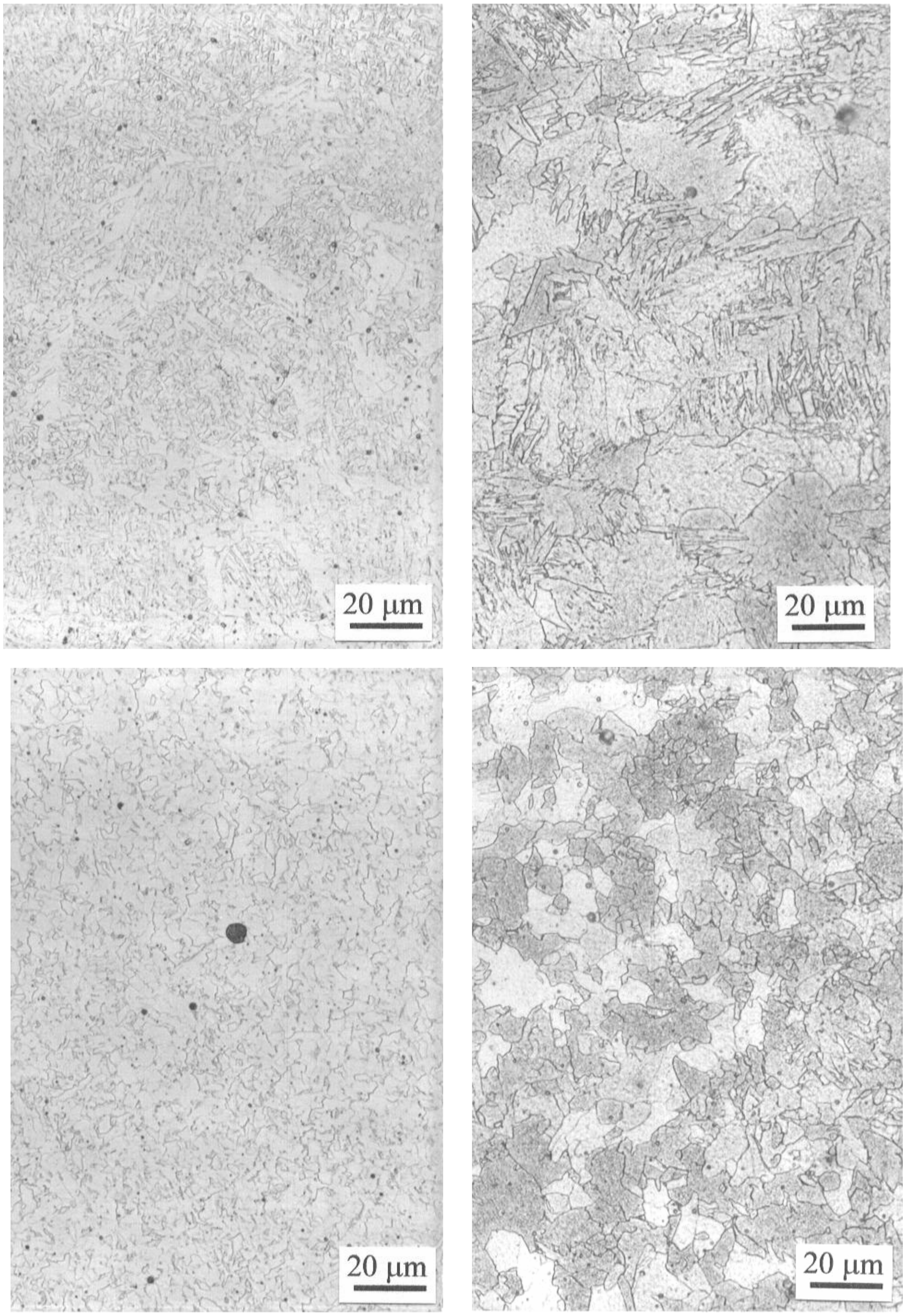

Figure 3.6.1: Reheated weld metal microstructures from 1T2B2 (left) and 1F3 (right) V-groove welds. The coarse-grained reheated zone appears at top, the fine-grained reheated zone appears in the bottom two photomicrographs.

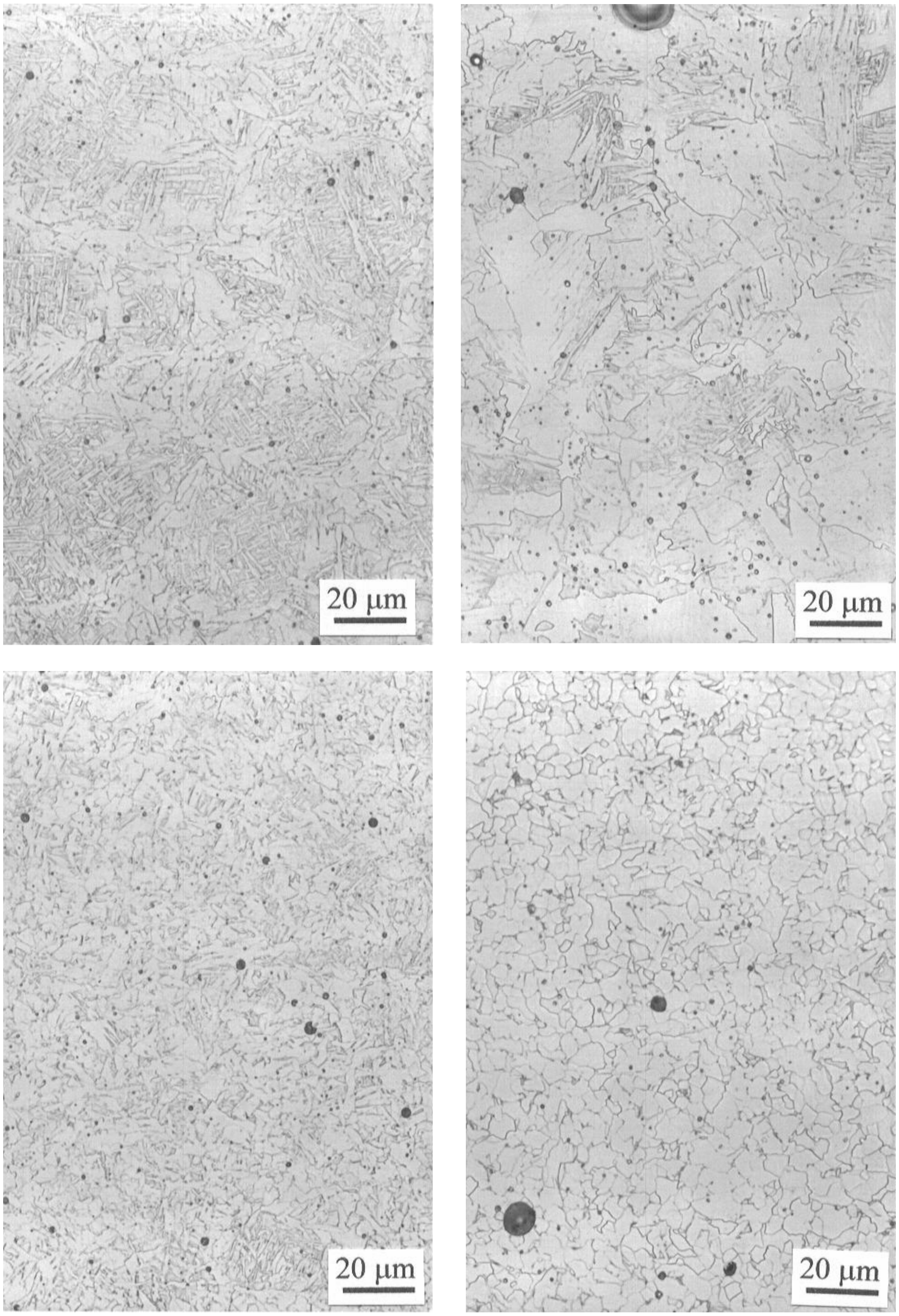

Figure 3.6.2: Reheated weld metal microstructures from 3T1B1 (left) and 3F3 (right) V-groove welds. The coarse-grained reheated zone appears at top, the fine-grained reheated zone appears in the bottom two photomicrographs.

3.7 Micro-Cracking:

Micro-cracking was observed to some extent in all of the BOP-BOB welds of Task I and Task II. Examples of micro-cracking can be seen in Figure 3.7.1. A similar type of cracking has been reported in the literature by Allen et al (1982) and Mota and Apps (1982). This type of cracking has been referred to as “chevron cracking” in its more severe form, or “micro-fissuring” in its less severe form. The cracking is caused by hydrogen in combination with the residual stress from welding (Allen et al 1982) (Mota and Apps 1982). Mota and Apps reported that the cracking tends to occur when the cooling rate below the transformation temperatures is high, and that the cracking can be eliminated by hydrogen control. It is not surprising that underwater wet welds suffer from this type of cracking due to the high hydrogen content and high cooling rates. In contrast to traditional views of hydrogen cracking, micro-fissuring has a tendency to occur in low-hardness microstructures, such as grain-boundary ferrite (Mota and Apps 1982).

Analysis of fracture surfaces from a bend-test specimen and a Charpy bar indicate that micro-cracks may be one of the features limiting the ductility of underwater wet welds. Figure 3.7.2 shows a feature from the bend-test fracture surface which strongly resembles the fractographic appearance of the micro-fissuring reported by Allen et al (1982) and Mota and Apps (1982). The central region appears to be a micro-crack which occurred in the primary weld metal, and was then reheated by the subsequent weld pass. The metallographic appearance of the micro-crack is probably similar to the cracks in re-heated weld metal shown in Figure 3.7.1 at bottom. According to Allen et al, thermal grooving appears on the fracture surface at the grain boundaries when the free surface is reheated. Thermal grooving is pointed out by the arrows in Figure 3.7.2, indicating that the central region was present in the primary weld metal and was re-heated by the subsequent weld pass. When the bend-test was performed, the micro-crack propagated initially by a brittle cleavage mechanism, then by ductile void coalescence.

Figure 3.7.3 shows another location on the bend-test fracture surface where a micro-crack propagated by a brittle cleavage. In Figure 3.7.3 the initial crack was oriented perpendicular to the bend-test fracture surface. Figure 3.7.4 shows a similar feature from the fracture surface of a 3F3 Charpy bar. In the case of the Charpy bar, the micro-crack did not propagate by cleavage initially. In the case of the bend-test, the slower strain rate allowed the micro-crack to propagate initially by hydrogen induced cracking. In the case of the Charpy bar, the high strain rate prevented initial propagation by hydrogen embrittlement.

The results of a quantitative survey of micro-cracking are presented in Figures 3.7.5 and 3.7.6. The amount of micro-cracking decreased as the volume percent porosity increased. Diffusible hydrogen may accumulate in pores, thereby reducing the diffusible hydrogen content and the occurrence of micro-cracking. The amount of micro-cracking increases significantly when the as-deposited weld metal hardness exceeds approximately 300 HV. Hardness is limited to 325 HV for a Class A weld, which is meant to prevent gross cracking. It may be advantageous to limit hardness to below 300 HV to minimize micro-cracking. Further reductions in hardness below 300 HV do not completely eliminate micro-cracking, as seen in Figure 3.7.6. To eliminate micro-cracking it will be necessary to control the weld metal hydrogen content or control the cooling rate below the transformation temperatures.

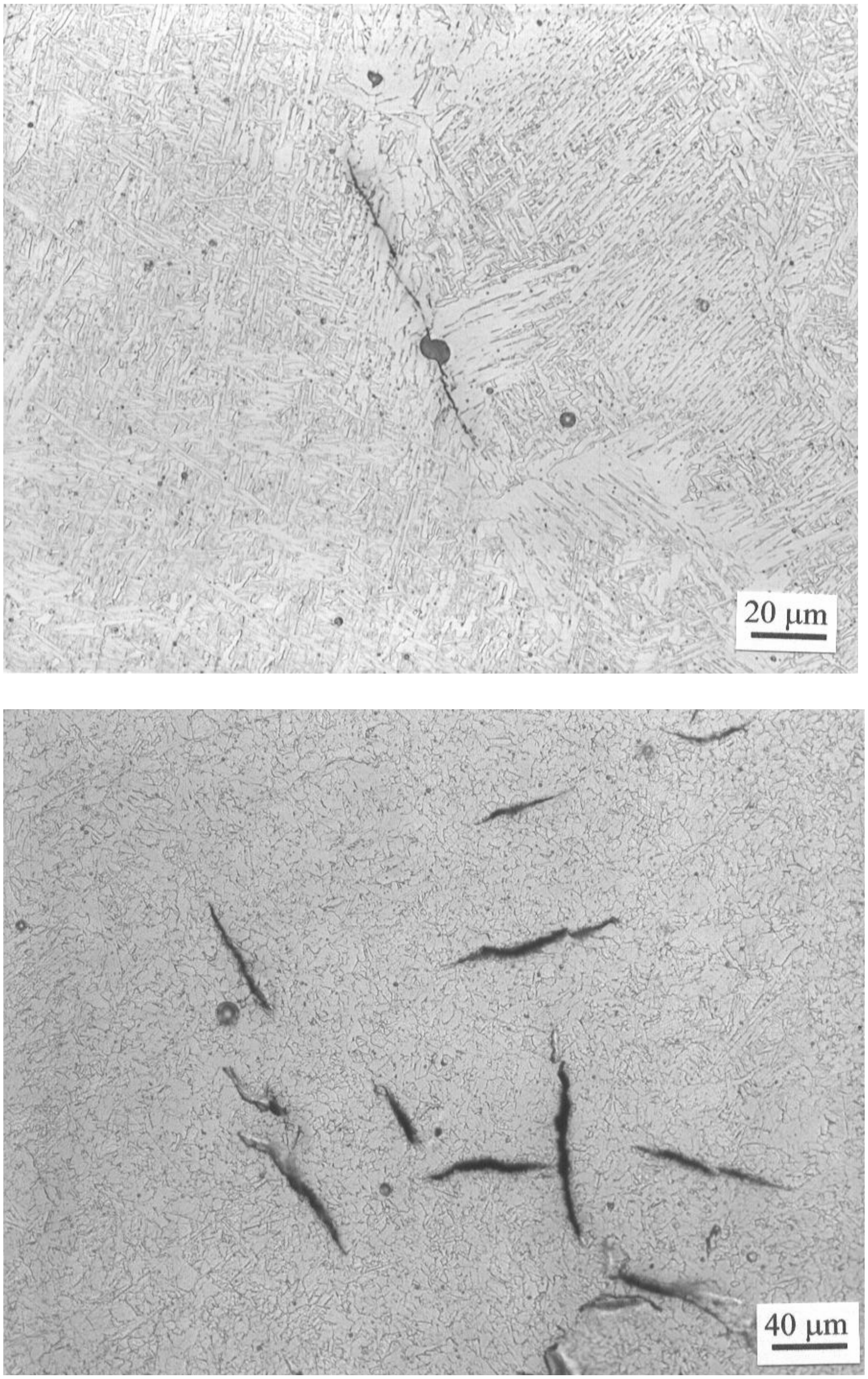

Figure 3.7.1: Micro-cracking in 1F3 as-deposited weld metal (top) and 2F3 reheated weld metal (bottom).

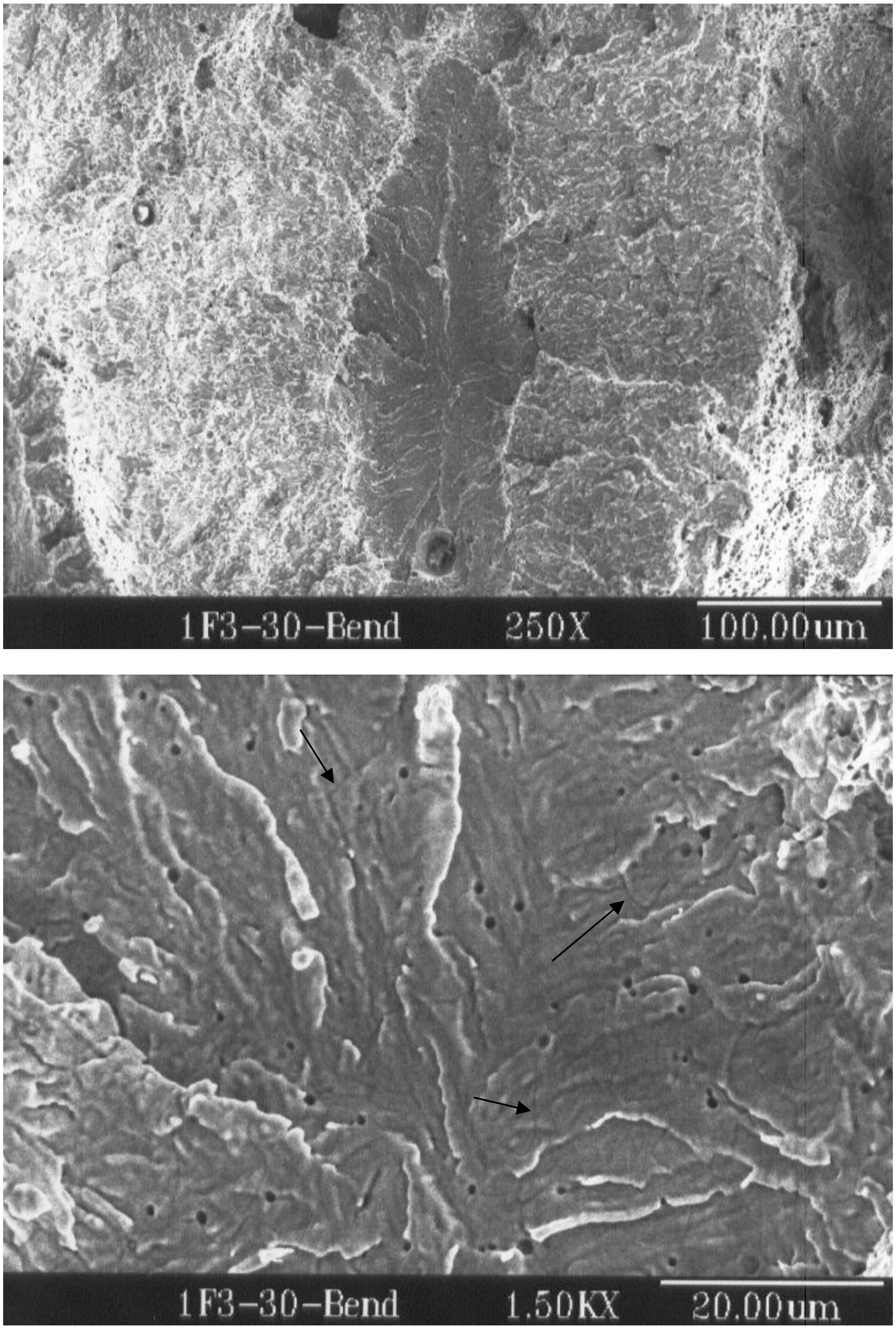

Figure 3.7.2: Micro-cracks acting as initiators of cracking on the fracture surface of a bend-test specimen from a 1F3 30 ft. V-groove weld. Top: a micro-crack (central region) propagated initially by brittle cleavage before changing to a ductile void coalescence mode. Bottom: High magnification view of the central region from above, showing thermal grooving (arrows)

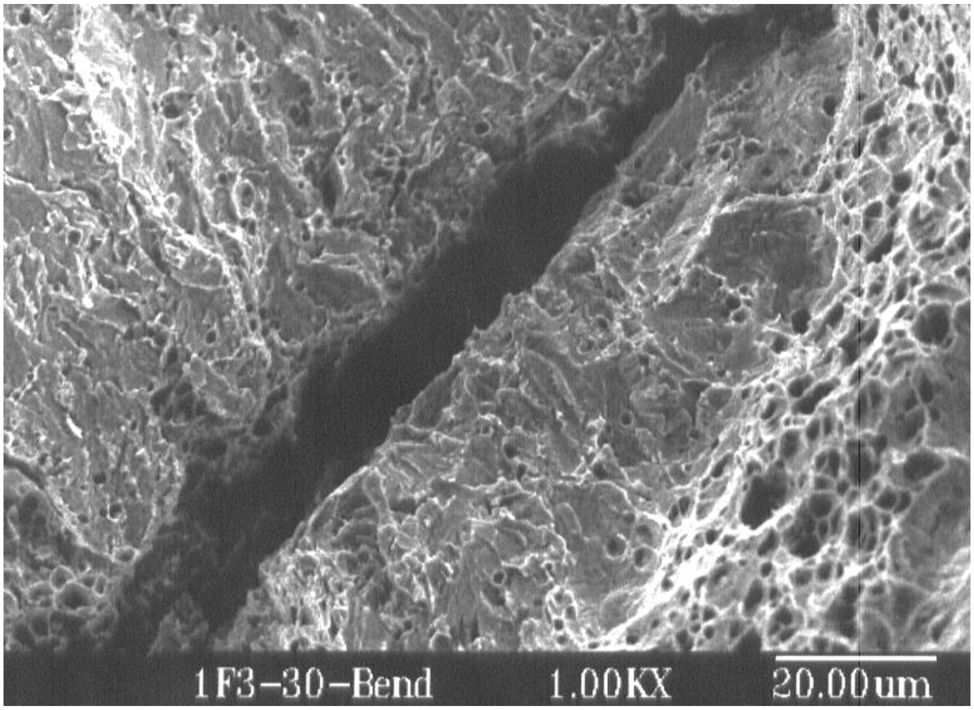

Figure 3.7.3: A micro-crack oriented perpendicular to the bend-test fracture surface acting as an initiation point for brittle fracture.

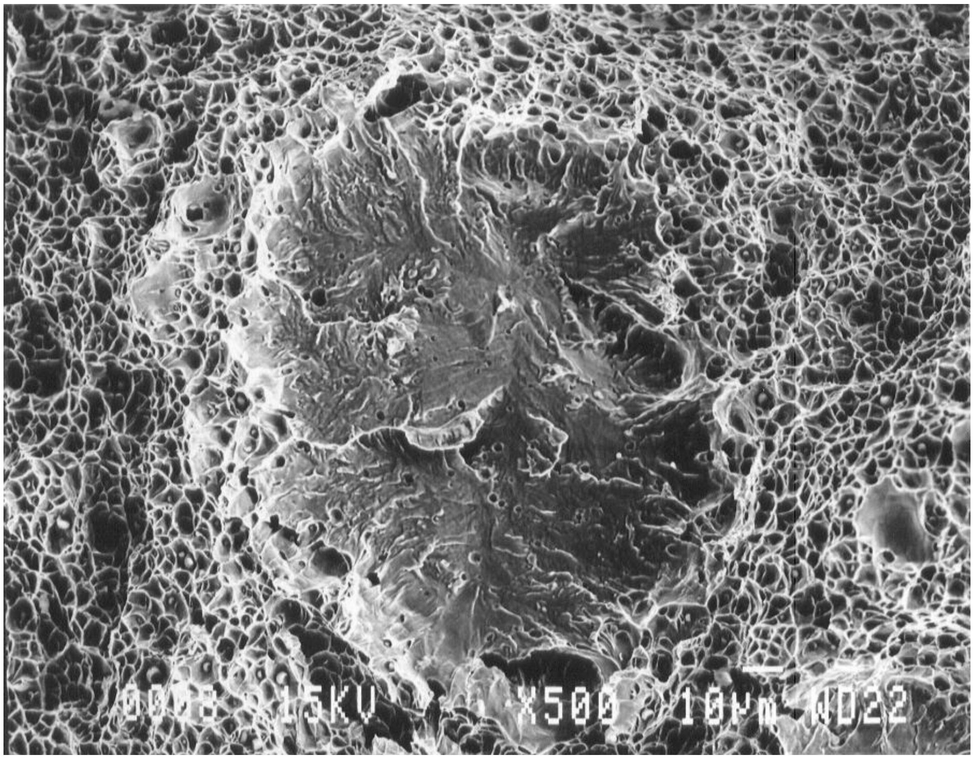

Figure 3.7.4: A possible micro-crack appearing on the fracture surface of a 3F3 Charpy bar.

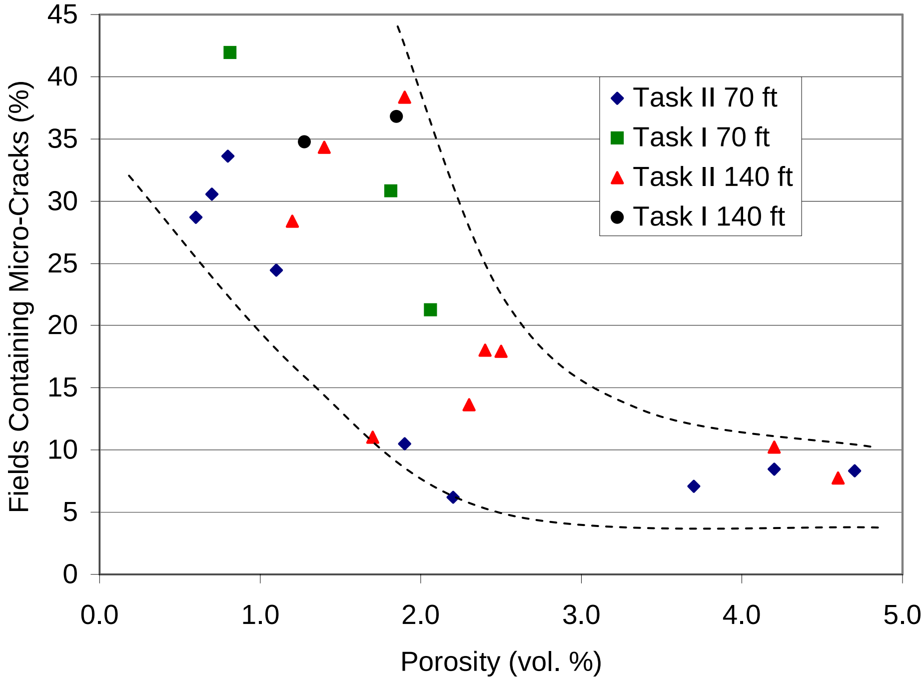

Figure 3.7.5: Percent of fields containing micro-cracks vs. volume percent porosity.

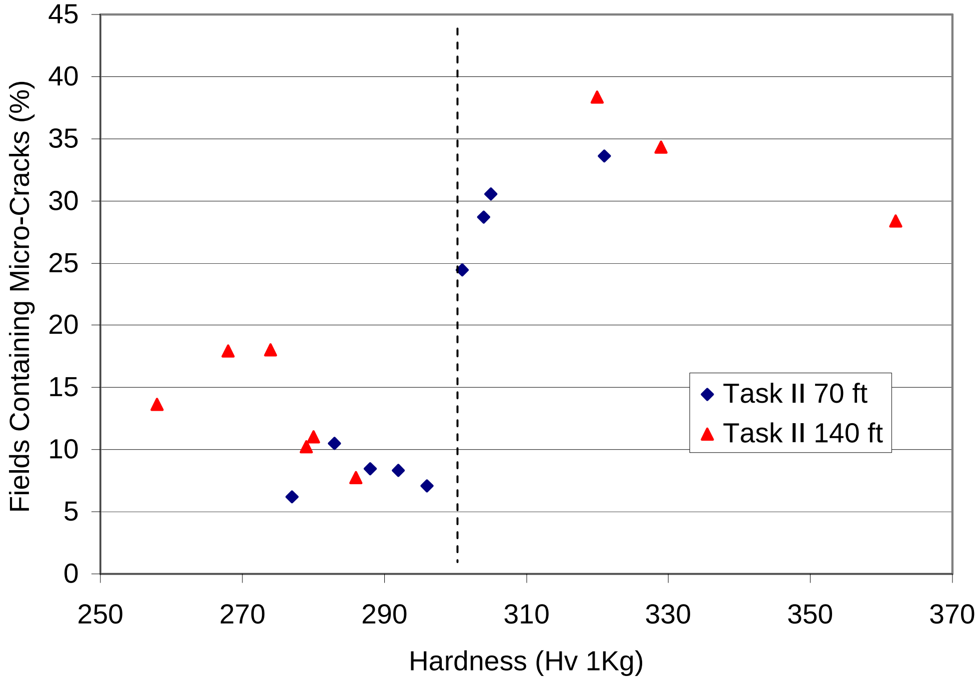

Figure 3.7.6: Percent of fields containing micro-cracks vs. top bead hardness.

3.8 Radiography:

All four of the Task IIB V-groove welds met AWS D3.6 Class A&B requirements. None of the V-groove welds from Task I met the Class A requirements. Cracking was observed on the Task I, 3F3 radiograph. Cracking was not observed in any of the Task II radiographs.

3.9 Mechanical Testing:

The mechanical testing results are summarized in Table 3.1.3. Results from Task I are given in Table 3.1.4 for comparison. Detailed information can be found in Appendix B.

Yield and tensile strengths were in all cases higher than in Task I, as seen in Figure 3.9.1. Ultimate tensile strengths were brought up above 60 ksi at 200 and 300 feet, which is a significant improvement over the low values from Task I. It is unclear why the 2T3B3 V-groove had a significantly higher tensile strength than the other Task II welds because the manganese content and hardness are comparable to the other welds while the level of porosity is even higher. Tensile elongation values were less than Task I at 70 and 140 ft., but improved over Task I for 200 and 300 ft.

Tensile elongation was greater than Task I welds at 200 and 300 ft., but was significantly less at 70 and 140 ft, as seen in Figure 3.9.2. Tensile elongation decreases with increasing yield strength. There was an increase in yield strength over Task I welds at 70 and 140 ft.; therefore, some decrease in elongation is to be expected. Elongation is also sensitive to the presence of porosity and micro-cracks, especially when small diameter tensile bars are used. The 2T3B3 V-groove weld had significantly higher porosity than the Task I weld. The 1T2B2 weld had an average hardness approaching 300 HV and may have had more micro-cracking than the Task I weld at 70 ft.

Charpy impact toughness values were similar to Task I in most cases, but slightly less than Task I at 70 ft, as seen in Figure 3.9.3. Fracture occurred by 90 to 100% ductile void coalescence in all cases, indicating that the measured toughness values are on the upper shelf of the Charpy toughness vs. temperature curve. Microstructural refinement is known to shift the ductile to brittle transition to lower temperatures, giving a greater margin of safety from brittle fracture. In this investigation, Impact toughness measurements were taken at one temperature; therefore, if any improvement in the transition temperature occurred, it was not observed. Upper shelf toughness is controlled by the concentration of defects, and is less sensitive to microstructure than the transition temperature. It is likely that the upper shelf toughness of underwater wet welds is limited by the high concentration of defects such as pores, oxide inclusions, and micro-cracks, and is not highly sensitive to microstructure.

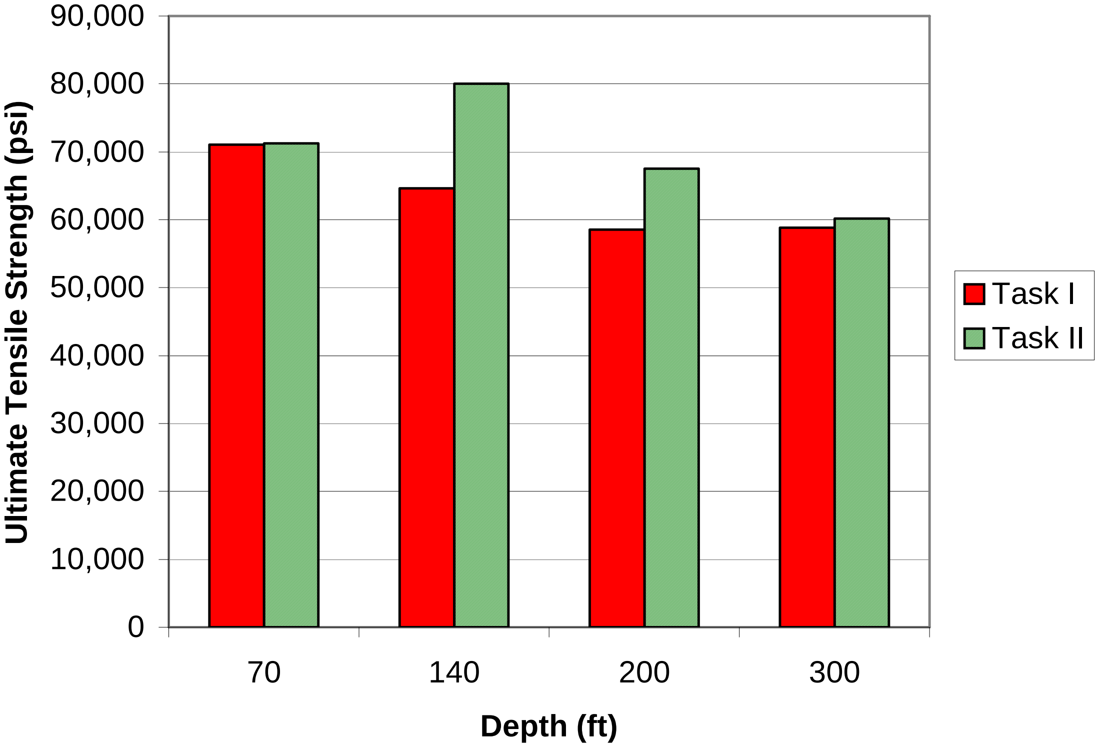

Figure 3.9.1: Ultimate tensile strength for Task I and Task II V-groove welds.

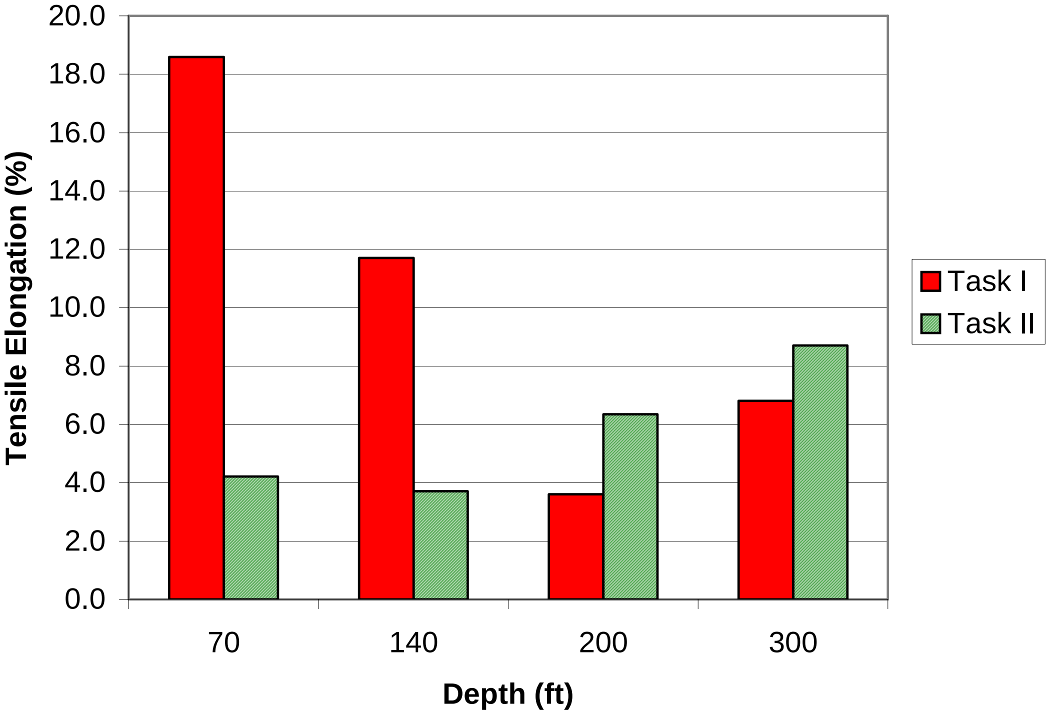

Figure 3.9.2: Tensile elongation for Task I and Task II V-groove welds.

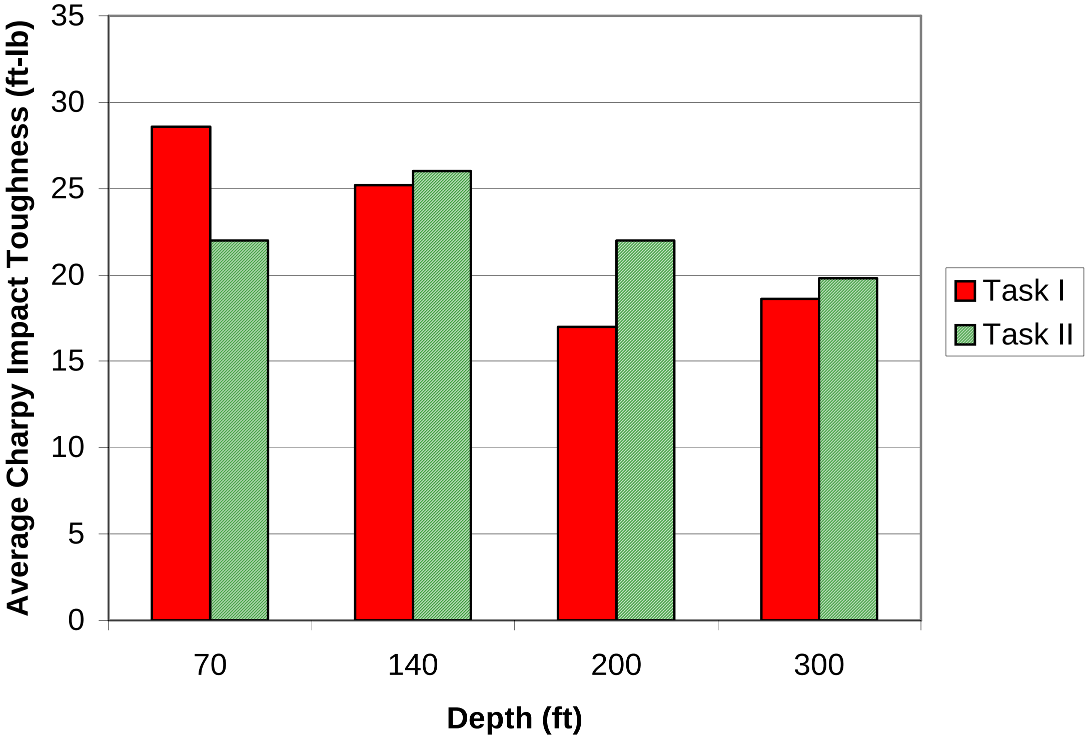

Figure 3.9.2: Average Charpy impact toughness for Task I and Task II V-groove welds.

4 CONCLUSIONS

1. Diver/welders reported that the electrodes performed well, and that slag removal was easy. There were no reports of problems with excessively fluid slag, as in Task I.

2. Increasing additions of ferro-titanium increased the recoveries of manganese and boron to the weld metal. It was possible to control the weld metal manganese content, which was not the case in Task I.

3. Switching from mechanical deposition to manual deposition of the test welds increased the recoveries of manganese and boron, decreased porosity, and reduced weld metal oxygen. The most likely explanation is decreased exposure of the weld pool to the water due to the ability of a skilled diver/welder to maintain a short arc length. It is possible that individual diver/welder skill may influence chemical composition and porosity in wet welds, particularly with micro-alloyed deposits.

4. Weld metal oxygen contents were similar for Task IA and Task IIA; however, weld metal oxygen was significantly decreased in Task IIB over Task IB values.

5. Weld metal nitrogen contents were not significantly increased by addition of titanium and boron.

6. Porosity increased with increasing additions of ferro-titanium and ferro-boron. One possible explanation is the effect of slag basicity on absorption of hydrogen into the weld pool, which limits the amount of hydrogen available to form porosity.

7. The fraction of acicular ferrite in the as-deposited microstructure was significantly increased in Task II (60-80%) over Task I values (10-20%).

8. Significant microstructural refinement was observed in the reheated weld metal of Task II compared to Task I V-groove welds.

9. Radiographs of all four of the Task II V-groove welds met AWS D3.6 Class A&B requirements.

10. Ultimate tensile strength values were increased for the Task II V-groove welds (60 to 80 ksi) over the Task I values (58 to 71 ksi).

11. Tensile elongation values were less than Task I at 70 and 140 ft., but improved over Task I at 200 and 300 ft.

12. Charpy impact toughness values were similar to Task I, except at 70 ft., where Task II values were slightly less. Upper shelf toughness values for underwater wet welds are most likely determined by defect concentration rather than microstructure.

5 ONGOING TASKS

Preliminary experiments with REM addition have been completed. Four formulations with increasing REM additions were extruded at CSM, and BOP-BOB welds were made at a depth of 1.5 ft. The effect of REM addition on weld metal oxygen content is shown in Figure 5.1. A reduction in weld metal oxygen content of 25% was observed with an addition of 3.2% Fe-Si-REM to the coating. It is known that upper shelf toughness in surface welds increases as weld metal oxygen content is reduced (Vishnu 1993). The recovery of all other alloying elements to the weld metal was increased with REM addition. The weld metal composition as a function of increasing REM addition is shown in Figure 5.2. The coating composition was held constant except for the increase in REM addition. Weld metal titanium content increased from 115 to 180 ppm and boron increased from 17 to 29 ppm over the same range of REM addition. REM is the strongest deoxidant in the system; therefore, it protects the other elements from oxidation.

Based on the data from the preliminary experiments, the REM test matrix was developed. Three levels of REM addition were tested at each depth. The selected levels of addition were 1.0, 2.5, and 4.0%. In the preliminary test, the lowest level of addition had no effect, therefore higher levels of addition were selected. The weld metal compositions of the selected formulations from Task IIA were targeted. The ferro-alloy additions were re-calculated to give the same weld metal composition as the selected Task II formulations, taking into account the effect of REM on recoveries. At the time of writing, some of the Task IIIA welds have been completed at Global, and are being shipped to CSM.

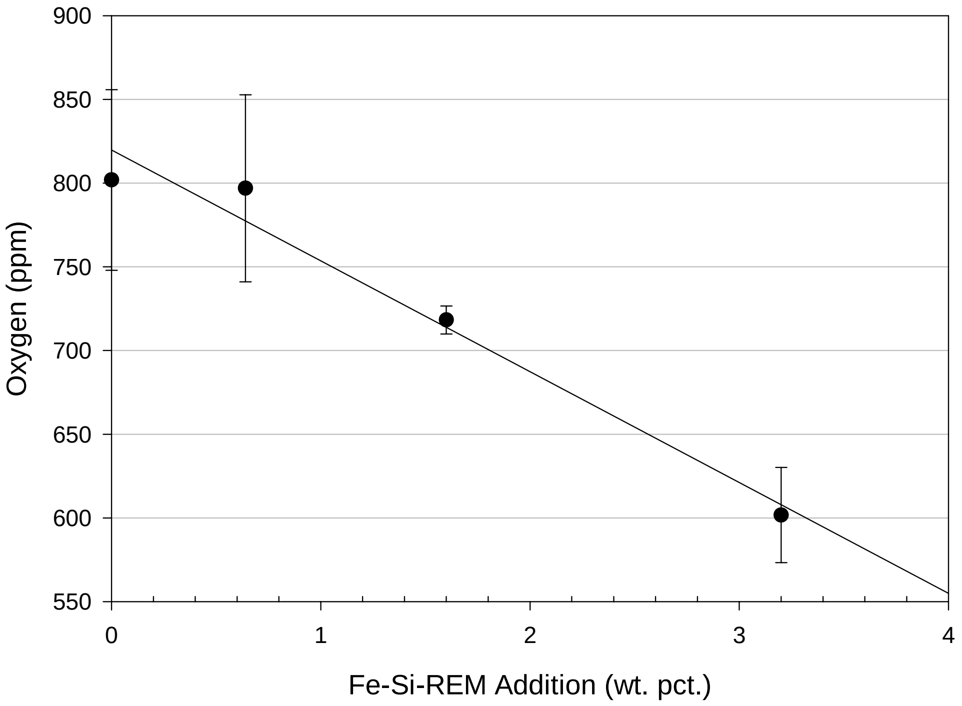

Figure 5.1: Effect of REM addition on weld metal oxygen content.

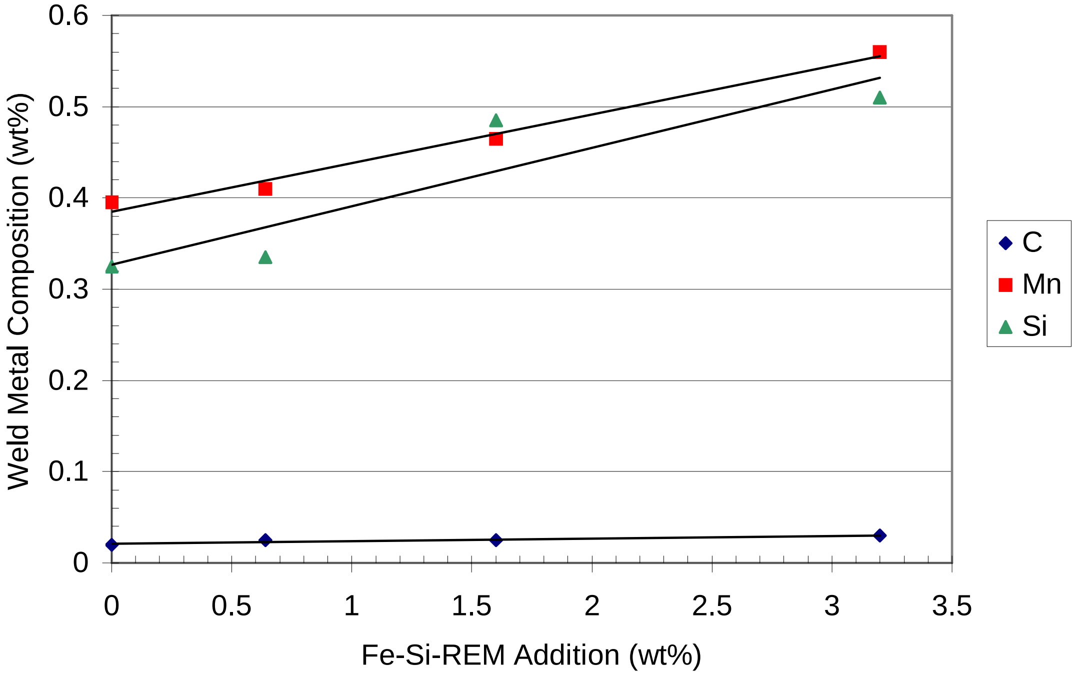

Figure 5.2: Effect of REM addition on weld metal composition with other coating ingredients held constant.

6 RESEARCH PERSONNEL

Prof. Stephen Liu – CWJCR – Professor of Metallurgical Engineering
Mr. Mark Rowe – MS candidate (BS Welding Engineering, Ohio State University)

REFERENCES

Allen, D. J., Chew, B., Harris, P. 1982. The Formation of Chevron Cracks in Submerged Arc Weld Metal. *Welding Journal*. 61(7): 212s-221s.

Evans, G. 1993. The Effect of Titanium in Manganese-Containing SMA Weld Deposits. *Welding Journal*. 72(3): 123s-133s.

Liu, S., Olson, D., Ibarra, S., 1994. Electrode Formulation to Reduce Weld Metal Hydrogen and Porosity. *Proceedings of the 13th Annual Conference on Offshore mechanics and Arctic Engineering, Vol III*. Houston TX pp. 291-298.

Medeiros, R., Liu, S., 1998. A Predictive Electrochemical Model for Weld Metal Hydrogen Pickup in Underwater Wet Welds. Journal of Offshore Mechanics and Arctic Engineering. 120(4): pp. 243-248.

Mota, J. M. F., Apps, R. L., 1982. "Chevron Cracking" – A New Form of Hydrogen Induced Cracking in Steel Weld Metals. Welding Journal. 61(7): 222s-228s.

Rissone, N., Bott, I., Jorge, J., Corvalan, P., Surian, C., 1997. ANSI/ AWS A5.1-91 E6013 Rutile Electrodes: The Effect of Wollastonite. Welding Journal. 76(11): 498s-507s.

Sanchez-Osio, A. 1994. The Influence of Consumable Composition and Solidification on Inclusion Formation and Growth in Low Carbon Steel Underwater Wet Welds. Thesis. Colorado School of Mines.

Sanchez-Osio, A., Liu, S., Ibarra, S. 1995. Designing Shielded Metal Arc Consumables for Underwater Wet Welding in Offshore Applications. *Journal of Offshore Mechanics and Arctic Engineering* 117(3): 212-20.

Suga, Y., Hasui, A., 1986. On Formation of Porosity in Underwater Wet Weld Metal. *IIW doc IX 1388-86*. American Council AWS. Miami FL.
Turkdogan, E. T. 1983. *Physiochemical Properties of Molten Slags and Glasses.* The Metals Society. London.

Surian, E. 1997. ANSI/ AWS E7024 SMAW Electrodes: The Effect of Coating Magnesium Additions. *Welding Journal*. 76(10): 404s-411s.

Turkdogan, E. T. 1983. *Physiochemical Properties of Molten Slags and Glasses.* The Metals Society. London.

Vishnu, P. R. 1993. Solid-State Transformations in Weldments. *ASM Handbook Vol. 6: Welding, Brazing, and Soldering.* ASM International. Metals Park, Ohio: 78.